Oxidation of amorphous HfNbTaTiZr high entropy alloy thin films prepared by DC magnetron sputtering

Hruška, P.; Lukáč, F.; Cichoň, S.; Vondráček, M.; Čížek, J.; Fekete, L.; Lančok, J.; Veselý, J.; Minárik, P.; Cieslar, M.; Melikhova, O.; Kmječ, T.; Liedke, M. O.; Butterling, M.; Wagner, A.;

Originally published:

November 2020

Journal of Alloys and Compounds 869(2021), 157978

DOI: https://doi.org/10.1016/j.jallcom.2020.157978

Oxidation of amorphous HfNbTaTiZr high entropy alloy thin films prepared by DC magnetron sputtering

Petr Hruška[1,2,*], František Lukáč[1,3], Stanislav Cichoň[2], Martin Vondráček[2], Jakub Čížek[1], Ladislav Fekete[2], Ján Lančok[2], Jozef Veselý[1], Peter Minárik[1], Miroslav Cieslar[1], Oksana Melikhova[1], Tomáš Kmječ[1], Maciej Oskar Liedke[4], Maik Butterling[4], and Andreas Wagner[4]

[1] Charles University, Faculty of Mathematics and Physics, V Holešovičkách 2, 180 00 Prague, Czech Republic
[2] Institute of Physics of the Czech Academy of Sciences, Na Slovance 2, 182 21, Prague, Czech Republic
[3] Institute of Plasma Physics of the Czech Academy of Sciences, Za Slovankou 3, 182 00, Prague, Czech Republic
[4] Helmholtz-Zentrum Dresden-Rossendorf, Institute of Radiation Physics, Bautzner Landstrasse 400, 01328 Dresden, Germany

*corresponding author: hruskap@fzu.cz

Keywords: high entropy alloys, HfNbTaTiZr, magnetron sputtering, X-ray photoelectron spectroscopy, positron annihilation spectroscopy

Abstract

High entropy alloys represent a new type of materials with a unique combination of physical properties originating from the occurrence of single-phase solid solutions of numerous elements. The preparation of nanostructured or amorphous structure in a form of thin films promises increased effective surface and high intergranular diffusion of elements as well as a high affinity to oxidation. In this work, we studied HfNbTaTiZr thin films were deposited at room temperature by DC magnetron sputtering from a single bcc phase target. Films exhibit cellular structure (~100 nm) with fine substructure (~10 nm) made of round-shape amorphous clusters. Films composition is close to equimolar with slight Ti enrichment and without any mutual segregation of elements. Oxidation at the ambient atmosphere leads to the formation of Ti, Zr, Nb, Hf, and Ta oxide clusters in the film up to the depth of 200 – 350 nm out of the total film thickness of 1650 nm. Oxygen absorption takes place preferentially in the large vacancy clusters located in between the amorphous cluster aggregates. The dominant type of defect is small open volumes with a size comparable with vacancy. The distribution of these defects is uniform with depth and is not influenced by the presence of oxygen in the film.

1. Introduction

High entropy alloys (HEA) called also complex concentrated alloys or multi-principal element alloys [1] are a group of materials with a combination of interesting properties. While most conventional alloys are based on one principal matrix element with alloying elements of lower

concentration, these alloys are a mixture of at least four elements in a similar atomic ratio. High configurational entropy of this system causes the formation of a single solid solution phase at high temperatures [2] and a high number of elements promises a combination of interesting phases when annealed [3]. Therefore, new combinations of physical properties are expected, namely mechanical, oxidation [4] and wear resistance [5].

HfNbTaTiZr alloy belongs to a group of refractory materials with a high melting point and thermal stability [4] with enhanced ductility and strength [6]. The casting of this alloy results in dendritic structure and subsequent homogenization annealing produces large grains and the alloy is susceptible to embrittlement from absorbed atmosphere impurities [7]. Moreover, local variations of the lattice parameter lead to the distribution of sizes of interstitials [1] forming an open structure favorable for hydrogen absorption. Interaction o refractory high entropy alloys with hydrogen have been widely studied [8, 9].

For hydrogen absorption in metals, a large surface area together with small grains microstructure is advantageous for diffusion along grain boundaries into the [10-12]. A nanocrystalline microstructure can be achieved by annealing of the amorphous phase. Amorphous alloys, often called metallic glasses are prepared either by high quenching rate of liquid phase or by various deposition techniques [13]. It was found that the composition of driven effects in sputtered thin films is decisive about the amorphization of the alloys, and the more complex is the composition of the alloy, the higher is the occurrence of amorphous content [14, 15]. A mechanism of phase selection in high entropy alloys between solid solution and amorphous phase was proposed based on atomic size dispersion and mixing enthalpy [16]. Therefore, it is interesting to prepare an amorphous phase from an alloy typical for single solution formation. Moreover, the hardness of such an amorphous thin film is much higher than bulk material [17]. Oxidation of amorphous or nanocrystalline film may block effective hydrogen absorption in the film though.

Two HfNbTaTiZr thin films with different thicknesses were prepared by DC magnetron sputtering. The deposition at room temperature is favorable for the formation of a nanocrystalline to an amorphous structure [18]. The effect of various deposition conditions (deposition rate, substrate temperature) and film composition to the structure of thin films prepared by magnetron sputtering was studied e.g. in [14, 19]. Oxidation of HEA films can be well studied by X-ray photoelectron spectroscopy combined with depth profiling [20]. Positron annihilation lifetime spectroscopy is a versatile tool providing information about open volumes, important for oxidation and hydrogen absorption properties, in both crystalline and amorphous structures.

2. Experimental

HEA films were prepared by DC magnetron sputtering in an ultra-high vacuum (UHV) deposition chamber. A DC power supply was operated at the power of 10 W, the voltage and

current lied in the range of 260 V – 200 V and 38 – 49 mA respectively resulting in a relatively slow deposition rate of approximately 6 nm/min. The base pressure in the UHV chamber of 10^{-7} – 10^{-8} Pa was ensured by a turbomolecular and an ion pump. The magnetron discharge was maintained in the Ar atmosphere at a constant pressure of 2 Pa, which was regulated by a needle valve, the Ar flow was fixed at 14 sccm. A single-phase round shape HfNbTaTiZr target with 1-inch diameter prepared by spark plasma sintering (SPS) from a gas atomized powder of HfNbTaTiZr alloy [21] was used as a sputtering target. The SPS processing of the target was performed at 1300°C for 2 min using a pressure of 100 MPa. The target exhibited a single bcc phase with the equiatomic composition, as confirmed by X-ray diffraction (XRD) and X-ray fluorescence (XRF), respectively.

HEA films were deposited on amorphous fused silica (FS) substrates with dimensions 10 × 10 mm^2, which were kept at room temperature (RT). The target to substrate distance was fixed at 100 mm. Samples with 2 different thicknesses, determined by transmission electron microscopy (TEM), were studied: (i) HEAM1 – 380 nm “thin” film and (ii) HEAM2 – 1650 nm “thick” film.

X-ray diffraction (XRD) analysis was carried out using Cu-Kα radiation on a Bruker Discover diffractometer equipped with a 1D LynxEye. XRD measurements were performed in the Bragg-Brentano symmetrical geometry. The TOPAS V5 code [22] was employed for the Rietveld refinement analysis of XRD spectra.

Lamellas for TEM investigation were prepared by focused ion beam (FIB) in a scanning electron microscope (SEM) ZEISS Auriga Compact. A protective platinum layer was deposited for the protection of the investigated layer before the preparation of the lamellas. TEM observations were performed on JEOL 2200FS operating at 200 kV. FEI Quanta 200F SEM equipped with energy dispersive X-Ray spectroscope (EDS) was employed for the mapping of chemical elements.

Atomic force microscopy (AFM) was employed to characterize the films’ surface morphology. AFM measurements were carried out at room temperature on an ambient AFM (Bruker, Dimension Icon) in Peak Force Tapping mode with ScanAsyst Air tips (Bruker, k = 0.4 N/m, nominal tip radius 2 nm). Measured topographies have 512 × 512 points resolution.

The films’ composition was investigated using XRF spectrometer Eagle III µProbe with a beam of 300 µm diameter.

X-ray Photoelectron Spectroscopy (XPS) analysis was performed in the Omicron NanoESCA instrument using a monochromatized Al-Kα radiation source (E = 1486.7 eV). Under these conditions, the information depth is a few nanometers. Elemental composition was calculated from peak areas employing photo-emission cross-section [23, 24]. For analysis of subsurface regions, depth profiling of the samples was enabled by an Ar^+ ion sputter gun in the preparation chamber of the NanoESCA instrument with the sputtering conditions E = 3 keV, pressure 2 × 10^{-4} Pa, and normal incidence angle.

Positron annihilation lifetime spectroscopy (PALS) was carried out on a pulsed slow positron beam MePS [25] operating at the ELBE (Electron LINAC with high Brilliance and low Emittance) facility [26] in the Helmholtz-Zentrum Dresden-Rossendorf. The energy of incident positrons in the beam was varied in the range from 1 to 16 keV, which corresponds to the mean positron implantation depth into HfNbTaTiZr ranging from 4 to 340 nm as calculated using the Makhovian implantation profile [27] and the theoretical bulk density of 10 g/cm^3 for the HfNbTaTiZr alloy [2]. Positron lifetime spectra were collected using a digital spectrometer [25] with a time resolution of 250 ps (FWHM of the resolution function). The decomposition of positron lifetime spectra into individual exponential components was performed using the PLRF code [28].

3. Results and discussion

3.1. Amorphous structure

The microstructure of films can be inspected in detail by TEM observations of cross-sections of the film lamellas cut by FIB. Figure 1a shows a TEM image of a cross-section of the HEAM1 film. The high-resolution image of the film layer in Figure 1b shows that no crystalline structure is present in the film. Indeed, the electron diffraction pattern from the region of the whole cross-section of the 380 nm thick film HEAM1 in Figure 1c proves that there is neither a crystalline phase nor a preferred orientation of nanocrystalline grains. The electron diffraction pattern exhibits a broad intensive ring surrounded by a diffusive halo. This is a typical pattern for amorphous structure. The amorphous structure of the HEA films deposited on FS at RT was confirmed also by XRD measurements.

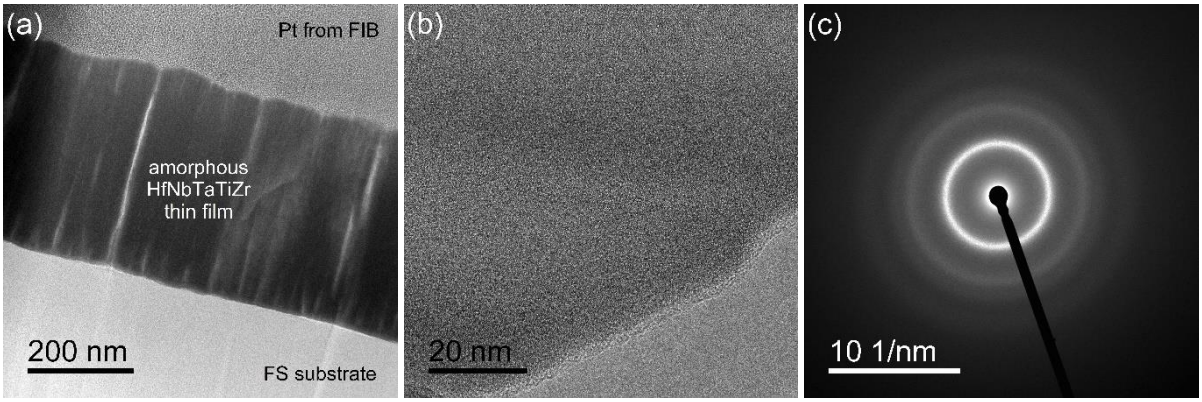

Figure 1: TEM measurements of the amorphous 380 nm thick HEAM1 film: (a) cross-section of the FIB cut lamella, (b) high-resolution TEM image of the HEA film layer, (c) electron diffraction pattern taken from the HEA film region.

Figure 2 compares XRD data measured in the symmetrical Bragg-Brentano geometry for HEAM1 and HEAM2 films and the electron diffraction pattern determined by TEM, i.e. radial profile of intensities from Figure 1c. The XRD pattern measured in the polycrystalline HfNbTaTiZr target is plotted in the figure as well for comparison. Single bcc structure with the lattice parameter a = 3.40835(2) Å agrees well with one of the authors' previous study [21]. The XRD patterns for both HEA films, HEAM1 and HEAM2, are similar to each other and are similar also to the electron diffraction pattern of HEAM1 measured by TEM, but clearly miss numerous reflections of the bcc phase present in the polycrystalline HfNbTaTiZr target. This effect cannot be due to the preferentially orientated growth of the HEA films, since the electron diffraction pattern in figure 1c shows no sign of texture in the circular pattern. Both X-ray and electron diffraction profiles are similar to a typical diffractogram of bulk metallic glasses, e.g. Zr-Cu-Al [29]. The first sharp diffraction peak, typical for metallic glasses, can be solely analyzed using peak broadening from the width of the Lorentzian curve and the coherence length can be calculated as 1.7(3) nm. Such value corresponds to the medium-range order in metallic glasses [30]. The amorphous diffusive halo at higher values of the scattering vector is split into few broad peaks visible in figures 1c and 2. Note that despite both X-ray and electron diffraction patterns look much alike, they are sensitive to different types of crystallographic planes, namely planes parallel with the substrate and planes perpendicular to the substrate for the XRD and TEM measurement, respectively. The similarity of the diffraction patterns measured by XRD and TEM, therefore, testifies that there is no preferential orientation of neither clusters nor cluster agglomerates, as observed by AFM, to the substrate in the HEA films.

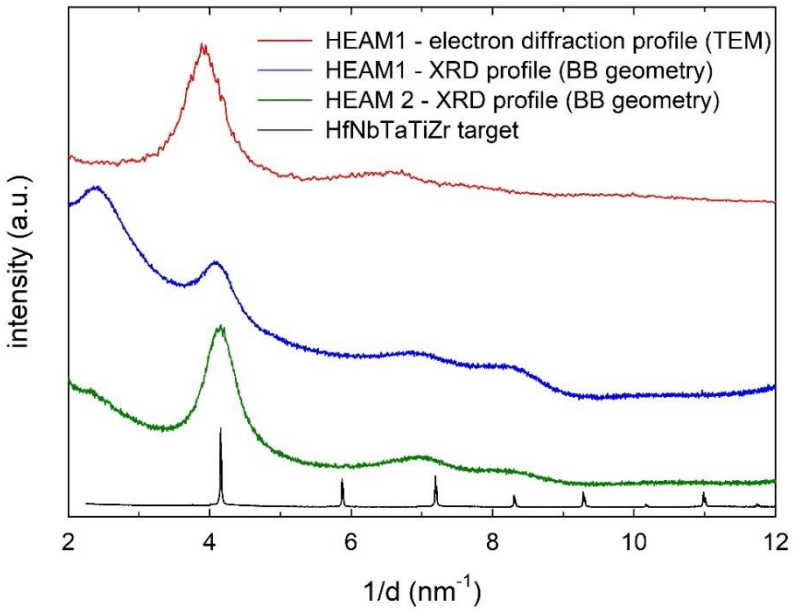

Figure 2: Comparison of the electron diffraction radial profile of the HEAM1 film and XRD profiles of HEAM1 and HEAM2 films measured in the symmetrical Bragg-Brentano (BB) geometry. XRD profile of the HfNbTaTiZr target prepared by SPS is included for comparison.

Figures 3a and 3b show AFM scans (area 5 × 5 μm^2) characterizing the morphology of the HEAM1 (thickness 380 nm) and HEAM2 (thickness 1650 nm) films. Details in higher magnification (area 1 × 1 μm^2) are shown in the insets. The RMS roughness R_q is listed in the top right corner of each scan. Note that R_q determined from larger scans is more accurate, since it is less affected by local deviations. Both films exhibit a very smooth surface which is a consequence of the slow deposition rate favoring smooth (atomic) layer-by-layer film growth. The roughness of the thicker film HEAM2 is 2-3 times higher compared to the thinner film HEAM1 while the thickness of the HEAM2 is more than 4 times higher than that of the HEAM1 film.

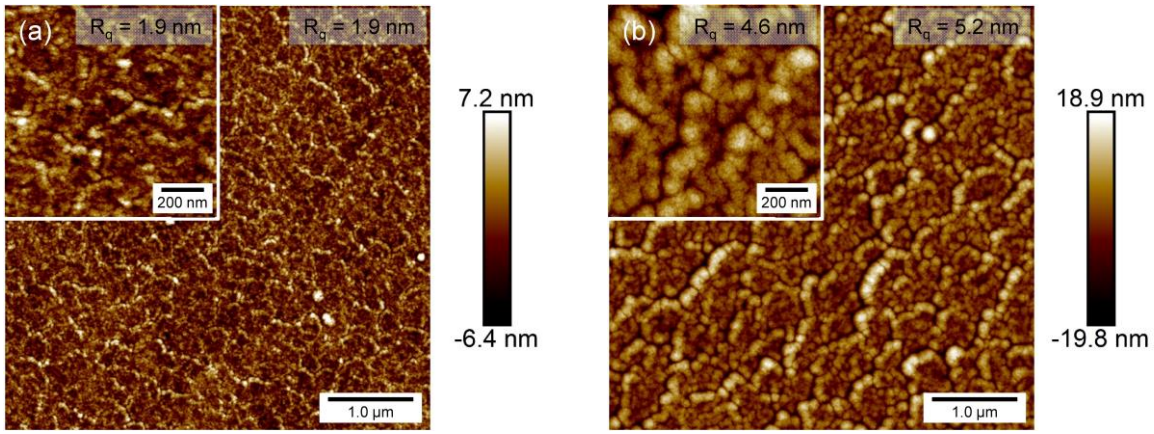

Figure 3: AFM measurement of (a) HEAM1 and (b) HEAM2 film, 5 × 5 μm^2 scans with 1 × 1 μm^2 detail. The surface roughness R_q is shown in each figure.

One can see in Figure 3 that the morphology of both films is very similar. The structure of HEAM2 film is more developed, as reflected by increased roughness, and consists of large aggregates, approx. 100 to 200 nm in size, separated by deep pits (dark regions in AFM scans). The aggregates consist of fine substructure with round-shape amorphous clusters, approx. 10 nm in size, see the inset in Figure 3b.

To investigate the fine substructure in detail, smaller scans containing 100 to 200 clusters were measured. Boundaries of clusters were manually identified and a surface area was evaluated for each region with a closed border. Using a round cluster approximation, cluster diameters were calculated. Histograms of cluster diameters for both films are shown in Figure 4 and can be reasonably approximated by the log-normal distribution. The mean cluster sizes for the HEAM1 and HEAM2 films were estimated to 15 nm and 13 nm respectively. Standard deviations given by FWHMs of log-normal distributions are 3 nm for both films. Therefore we can say that the aggregate structure develops with the film thickness, as reflected by increasing roughness, while the aggregate substructure virtually remains the same independently on the film thickness.

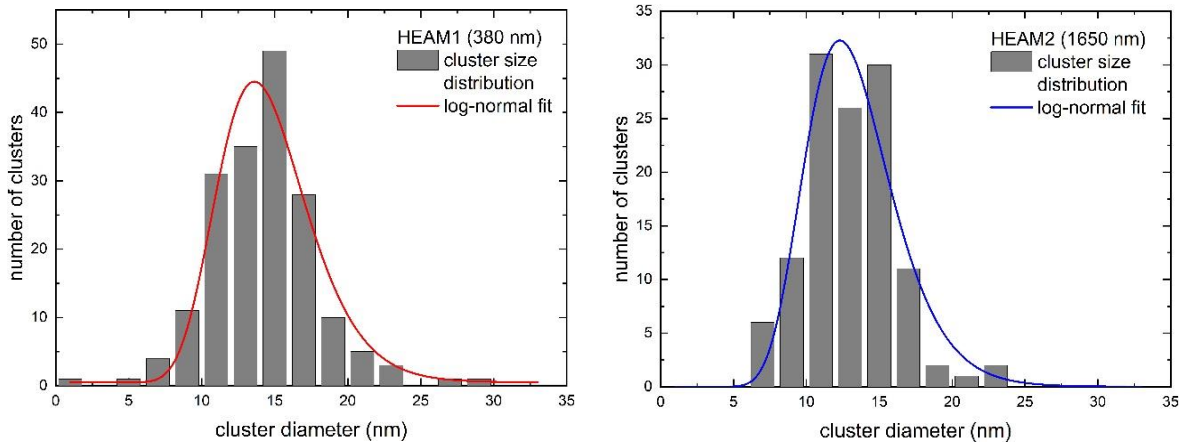

Figure 4: Histograms of cluster diameters for HEAM1 and HEAM2 films approximated by the log-normal distribution.

3.2. Oxidation of amorphous films

EDS analysis showed high oxygen content significantly exceeding the possible contribution of the FS (SiO_2) substrate. Considering the fact that the films were deposited under UHV conditions, the only possible source of such a high concentration of oxygen is the exposure to the ambient atmosphere during the transport and the storage of the films. Unlike bulk HfNbTaTiZr alloys prepared by conventional arc melting, which exhibit typical dendritic structure, EDS mapping of HEA films showed no segregation of Hf, Nb, Ta, Ti, Zr elements. Figure 5 shows EDS maps of the HEAM2 film, each point corresponds to an area with 60 nm diameter. Therefore, we can say the films are homogeneous on the scale larger than 100 nm, which is comparable with the size of the aggregate structure observed by AFM.

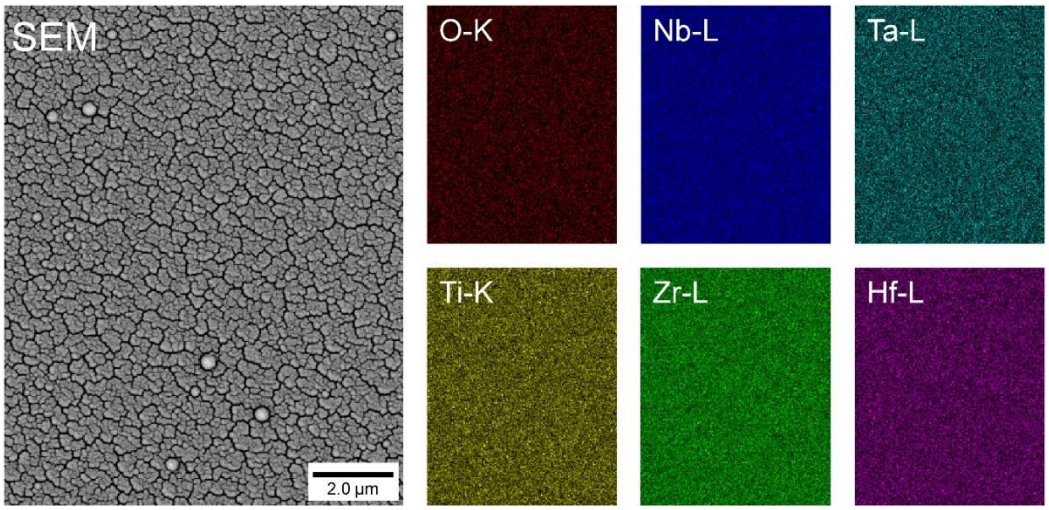

Figure 5: SEM picture (back-scattered electrons) and corresponding EDS maps of the O, Nb, Ta, Ti, Zr, and Hf elements for the HEAM2 film surface. K-lines were analyzed for O and Ti, L-lines were analyzed for Nb, Zr, Ta, and Hf.

The composition of HEA films was characterized by the XRF method. Note that XRF can be used for reliable determination of the concentration of chemical elements with Z > 10, i.e. it is not sensitive to oxygen content. The results of the XRF chemical analysis of HEAM1 and HEAM2 films are listed in Table 1. The results of the XRF chemical analysis of the HfNbTaTiZr target before and after sputtering are included in the table as well. The XRF spectra were treated within a model without calibrated standards, i.e. phenomena like X-ray absorption, self-excitation, and finite film thickness, were approximated by empirical formulas. Variation of atomic concentrations obtained by such a model is typically 2 – 5 at. %, depending on the parameters of the XRF model. Note that using a calibrated samples as standards can improve the precision of the XRF analysis 10 – 100 times and will be necessary for the authors' following studies concerning the composition of HEA films.

One can see in Table 1 that the composition of HEAM1 and HEAM2 films is, within the precision of the XRF analysis, close to the equimolar composition of the HfNbTaTiZr alloy. However, the HEAM1 film is enriched with Ti, while the HEAM2 film is depleted with Ti. The reason for this discrepancy is as follows. The first HEAM1 film was deposited from the original equimolar HfNbTaTiZr target. Ti enrichment of the film is caused by preferential sputtering of the Ti as the element with the lowest atomic mass. Simultaneously the target was depleted in Ti, as confirmed by the XRF analysis of the sputtered target. Therefore, the sputtering of the Ti depleted target leads to the lack of Ti in the following samples, particularly the HEAM2 film.

Element		**Ti**	**Zr**	**Nb**	**Hf**	**Ta**
XRF analysis						
K-line energy (keV)		4.510	15.776	16.617	55.801	57.450
L-line energy (keV)		0.452	2.042	2.166	7.898	8.145
composition* (at. %)						
HEAM1	as-deposited	23	19	19	18	21
HEAM2	as-deposited	18	21	21	19	21
HfNbTaTiZr	target before dep.	20	20	20	20	20
HfNbTaTiZr	target after dep.	12	22	23	20	23
sputtering						
atomic number		22	40	41	72	73
atomic mass		47.880	91.220	92.906	178.49	180.948
sputtering yield (at. per ion)**		0.577	0.632	0.634	0.748	0.664

* Only Ti, Zr, Nb, Hf, Ta elements were taken into account.

** Sputtering yields for normal incidence of Ar^+ ions with 500 eV energy [31-33].

Table 1: Chemical composition in at. % as determined by XRF for amorphous HEAM1 and HEAM2 films and HfNbTaTiZr target before and after deposition. K-lines were analyzed for Ti, Zr, and Nb, L-lines were analyzed for Hf and Ta. Atomic numbers, atomic masses, and sputtering yields [31-33] in the number of atoms per Ar^+ ion are included.

Sputtering yields in Ar for the normal incidence for Ti, Zr, Nb, Hf, Ta are among the lowest across the periodic table [31-33]. Further, within these five elements, the actual values of the yield are very comparable, see Table 1, which favors the near-equimolar composition of the deposited film. Note that values in Table 1 correspond to the sputtering of pure materials and does not take into account mutual bonds in the HfNbTaTiZr alloy. The preferential sputtering of Ti, therefore, seemingly contradicts its lowest sputtering yield compared to the other elements and is presumably the result of the lowest atomic mass of Ti.

XPS spectra for the HEAM2 film, which are shown in Figure 6, were fitted in the KolXPD software using Shirley background and Voigt peaks for O 1s or Voigt doublets with appropriate spin-orbit splitting for metal oxides. Metallic states of the same core levels with highly asymmetric profiles were fitted with Doniach-Šunjić doublets convoluted with Gaussian function instead. Metal oxide signal contributions are identified as peaks shifted to higher binding energies in comparison with the metallic peaks; the larger is the chemical shift, the higher is the oxidation number. Peak parameters and their chemical shifts are consistent with the literature [24, 34-40].

core level	Ti $2p_{3/2}$	Nb $3d_{5/2}$	Zr $3d_{5/2}$	Ta $4f_{7/2}$	Hf $4f_{7/2}$	O 1s
reference values – binding energy (eV)						
metal	453.94	202.31	178.75	21.80	14.28	--
metal – LW	0.25	0.07	0.09	0.03	0.04	--
highest oxide	TiO_2 458.5 - 459.3	Nb_2O_5 207.3 - 208.2	ZrO_2 182.0 - 183.4	Ta_2O_5 26.3 - 27.2	HfO_2 16.6 – 17.9	--
HEAM2 as deposited – binding energy (eV)						
metal		202.9	179.2	22.5	14.5	***531.4***
metal oxide	458.5	**208.4**	**183.4**	**27.1**	**18.0**	*532.4*
	459.8	207.0				
HEAM2 after 7h depth profiling – binding energy (eV)						
metal	**454.1**	**202.6**	**178.9**	**22.1**	**14.2**	***531.4***
metal oxide	454.9	203.1	**179.7**	22.7	14.8	*533.1*
		203.4	183.7	27.4	18.0	*535.1*

Table 2: Binding energies in eV of metals' [34, 35] and metal oxides' [37, 38] major core levels frequently used for XPS analysis. The standard deviation of values in [34] is 0.06 eV, LW is the Lorentz natural line width [35]. Bold values correspond to the position of the dominant peak in the measured XPS spectrum.

As revealed by XPS, the surface region of the HEAM2 film is oxidized. All deposited elements are present in a form of oxides, the oxygen content was determined to 66 at. %. No oxide particles were observed by SEM, TEM nor XRD though. Thus, we assume the present oxides are ordered on a short-range scale of few nm only. The real surface of the metallic film typically contains adsorbents from the ambient atmosphere and an oxide-based passivation layer [41, 42]. The presence of ambient adsorbates is reflected in the carbon content of 12 at. % in the as-deposited film, while a high oxygen content corresponds also to the passivation layer.

To investigate the oxidation with a depth resolution, a standard depth profiling using Ar^+ sputtering in the XPS apparatus was performed. After 1 h of depth profiling, a 30 – 50 nm thick layer was removed from a region probed by XPS and the oxygen concentration slightly decreased to 48 at. %. The oxide states of elements diminished in favor of metallic states. Virtually all Nb and Ta atoms were already in the metallic state. On the contrary, Ti and particularly Zr and Hf atoms remained both in the oxide and the metallic states. This is due to the high affinity of these elements to oxygen given by their electronegativity, bond energy, crystal cohesive energy, etc., as described in [43-45].

After 7 h of depth profiling, a 200 – 350 nm thick layer was removed and oxygen content dropped to 18 at. %. Ti, Zr, and Hf atoms were present predominantly in metallic states. Nevertheless, the oxide and sub-oxide states of these elements were still present. Hf and Zr exhibit a high amount of sub-oxide states attributed to the first stage of Zr and Hf oxidation into ZrO_x- and HfO_x-like states due to the high affinity of these elements to dissolved oxygen [37-40].

Therefore with increasing depth oxygen content is gradually decreasing. Absorbed oxygen atoms are preferentially bonded to Ti, Zr, and Hf more likely than to Nb and Ta. However, in higher depths, the film has a metallic character. The relatively high oxygen content in higher depths shows oxygen was able to diffuse through the passivation layer. This was enabled by an open structure of the amorphous film acting as a getter. Oxygen diffusion into polycrystalline HEA films studied by XPS depth profiling was reported in [20].

Atomic concentrations of the deposited elements as determined by XPS fall into the range of (20 ± 10) at. %. The more precise composition is provided by the XRF analysis as a method less sensitive to the surface, which may, in general, exhibit deviations from the bulk composition. Moreover, depth profiling by Ar^+ sputtering is accompanied with many effects, which alter the

composition of the studied material as well. Consequently, uncertainties in the obtained compositions must be taken into consideration [46].

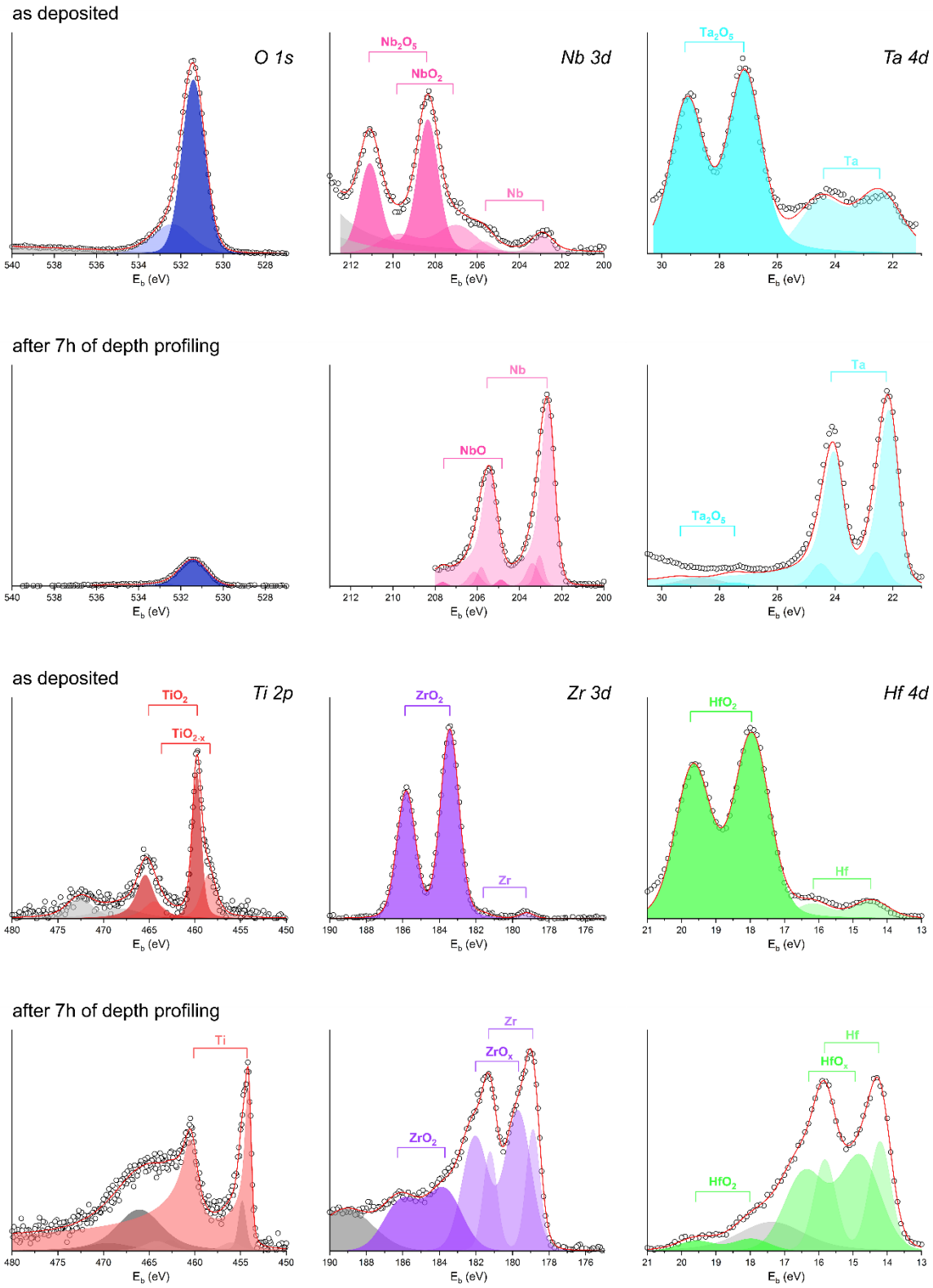

Figure 6: High-resolution XPS spectra of elements present in HEAM2 film measured in the as-deposited state and after 7 h of depth profiling. Measured data (open points) correspond well

to the fit (red line). Positions of doublets for metal and oxide states are marked with horizontal lines.

The defect structure of a 1650 nm thick HEAM2 film was investigated by positron annihilation lifetime spectroscopy. The positron implantation profile is described by the asymmetric Makhovian distribution. Both mean implantation depth $\bar{z}$ and FWHM w increase with positron energy with a power factor of 5/8. For simplicity, we propose using the interval $(1/2\,\bar{z}, 3/2\,\bar{z})$ to characterize the region, which contains 65 % of all implanted positrons. For the maximal positron energy of 16 keV, less than 10^{-7} % of all positrons penetrated the FS substrate. Therefore, all positrons annihilated in the volume of the film. Moreover, comparable depths of the HEAM2 sample were probed by the PALS and the XPS methods.

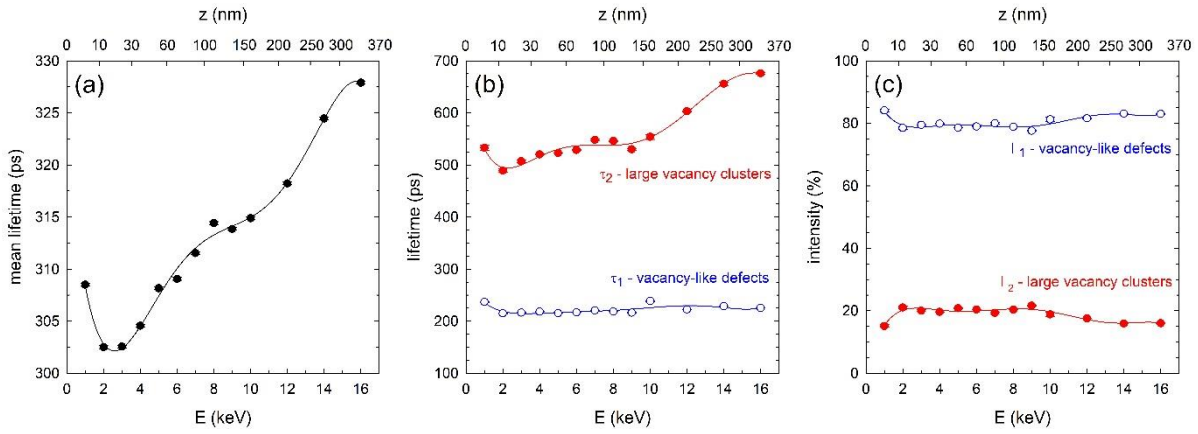

Figure 7: Positron annihilation lifetime measurements for the 1650 nm thick HEAM2 film plotted as a function of the energy of incident positrons, the mean positron penetration depth is depicted at the top axis. (a) Development of the mean positron lifetime, (b) positron lifetime components and (c) their corresponding intensities.

In general, the mean positron lifetime $\bar{\tau}$ is a robust parameter, which is not influenced by mutual correlation among fitting parameters. Hence, the development of $\bar{\tau}$ provides an insight into the defect depth profile in the sample. Figure 7a shows $\bar{\tau}$ plotted as a function of the energy of incident positrons E, previously published in the authors' work [47]. For all energies the values of $\bar{\tau}$ exceed 300 ps, which is a much higher value than the bulk lifetime of 146 ps for HfNbTaTiZr alloy [48-50]. This is caused by vacancy-like open-volume defects, which are present in large concentrations and are able to trap thermalized positrons.

At very low energies (up to 1 keV) almost all positrons annihilated in the surface state. With increasing energy, positrons penetrate deeper into the HfNbTaTiZr layer, and a fraction of positrons diffusing back to the surface gradually decrease, which results in a decrease of $\bar{\tau}$. At higher energies (above 3 keV) $\bar{\tau}$ monotonically increase with energy. This increase of the mean

positron lifetime can be caused either by increasing concentration of vacancy-like defects or by an increase of their mean size.

To obtain a better insight to PALS data, for each positron energy the positron lifetime spectrum was decomposed into two exponential components: (i) short-lifetime component $\tau_1 \approx 220$ ps with intensity $I_1 \approx 80$ %; (ii) long-lifetime component $\tau_2 \gtrsim 500$ ps with intensity $I_2 \approx 20$ %. The development of lifetimes and intensities of both components with energy E is shown in Figures 7b and 7c. Since lifetimes of both components are substantially higher than the bulk lifetime for the HfNbTaTiZr alloy, the concentration of defects in the HEAM2 film is so high that all positrons are annihilated in the trapped state (saturated positron trapping).

According to *ab-initio* calculations, the lifetime of a positron trapped in a monovacancy in the bcc-HfNbTaTiZr lattice is 212 ps. Therefore, the shorter component τ_1 corresponds to positrons trapped in small open-volume defects with a size comparable with monovacancy. The values of lifetime τ_1 and intensity I_1 virtually does not change with depth. In context with the AFM observations, we assume positrons are predominantly trapped in open spaces between amorphous clusters with the mean size of 13 nm.

The longer component τ_2 comes from positrons trapped in large vacancy clusters and voids between the ~100 nm large aggregates, which were observed by AFM. Note that the maximum theoretical lifetime of positrons annihilating in large vacancy clusters is 500 ps. Thus, the long-lifetime component τ_2 includes also pick-off annihilations of ortho-positronium (o-Ps) with a typical lifetime of ~1 ns, in particular for the energies of 12 keV and higher.

The constant intensity of the long-lifetime component means the concentration of inter-aggregate voids is approximately constant with depth, which is in a good agreement with AFM observations. However, increasing lifetime τ_2 implies an increasing volume of inter-aggregate voids. This effect is likely connected with oxygen absorption in these voids. The XPS analysis revealed there is a high concentration of oxygen in the HEA films which strongly decreases with the depth. Hence, it is likely that voids in the sub-surface region are filled by oxygen atoms which effectively reduce its free volume and, thereby, also the lifetime of positron trapped inside the void. Alternatively, the presence of oxygen and oxides in the voids' walls can effectively prevent the formation of the positronium leading to a shortening of the lifetime.

One can see in Figure 8 the lifetime τ_2 is virtually constant up to the depth of 150 nm. It means in this sub-surface region the inter-aggregate voids are likely saturated with oxygen. With increasing depth τ_2 begins to grow due to reduced oxygen concentration inside voids. This is in very good agreement with XPS observations. Note that constant lifetime τ_1 and intensity I_1 indicate no significant oxygen absorption inside the amorphous structure. Thus, oxygen contamination occurs on the interfaces among aggregates only.

4. Conclusions

The amorphous structure and oxidation of HfNbTaTiZr thin films were investigated. Two HfNbTaTiZr films with thicknesses of 380 nm and 1650 nm were deposited at room temperature on fused silica substrates by DC magnetron sputtering from a single bcc phase target prepared by spark plasma sintering. The amorphous structure with no long-range ordering of atoms was confirmed by TEM and XRD observations. Both films exhibit similar morphology with ~100 nm aggregates made of ~10 nm round-shaped clusters. Close-to-equimolar composition with slight Ti enrichment and no mutual segregation of elements was observed by XRF and EDS. Oxidation of the films was studied by XPS combined with depth profiling. Oxygen absorbed from the ambient atmosphere reacted with Ti, Zr, Nb, Hf, and Ta atoms and formed oxide and sub-oxide nanoclusters. The oxygen-contaminated layer with a thickness of approximately 200 – 350 nm, out of the total film thickness of 1650 nm, contains predominantly Ti, Zr, and Hf oxides. Two types of open volumes, uniformly distributed with depth, were observed by positron annihilation lifetime spectroscopy. Smaller defects with a size comparable with monovacancy in bcc HfNbTaTiZr structure are the dominant type of defect and are not influenced by oxygen content in the film. Larger open volumes located in between the aggregates of amorphous clusters are a dominant region, where oxidation of the film takes place.

5. Acknowledgments

This work was supported by the Czech Science Foundation (project 17-17016S). P. Hruška acknowledges the support of the PPLZ project of the Czech Academy of Sciences. We acknowledge the Operational Program Research, Development and Education financed by European Structural and Investment Funds and the Czech Ministry of Education, Youth and Sports (Project SOLID21 CZ.02.1.01/0.0/0.0/16_019/0000760). Author P. Minárik acknowledges partial financial support by ERDF under project No. CZ.02.1.01/0.0/0.0/15 003/0000485. The MePS facility has partly been funded by the Federal Ministry of Education and Research (BMBF) with the grant PosiAnalyse (05K2013).

References

1. Miracle, D.B. and O.N. Senkov, *A critical review of high entropy alloys and related concepts.* Acta Materialia, 2017. **122**: p. 448-511.
2. Senkov, O.N., et al., *Microstructure and room temperature properties of a high-entropy TaNbHfZrTi alloy.* Journal of Alloys and Compounds, 2011. **509**(20): p. 6043-6048.
3. Cantor, B., *Multicomponent and High Entropy Alloys.* Entropy, 2014. **16**(9): p. 4749-4768.
4. Senkov, O.N., et al., *Microstructure and elevated temperature properties of a refractory TaNbHfZrTi alloy.* Journal of Materials Science, 2012. **47**(9): p. 4062-4074.

5. Islak, S., et al., *Wear properties and synthesis of CrFeNiMoTi high entropy alloy coatings produced by TIG process.* Indian Journal of Engineering & Materials Sciences, 2020. **27**: p. 659-664.
6. Zýka, J., et al., *Microstructure and Room Temperature Mechanical Properties of Different 3 and 4 Element Medium Entropy Alloys from HfNbTaTiZr System.* Entropy, 2019. **21**(2).
7. Dirras, G., et al., *Elastic and plastic properties of as-cast equimolar TiHfZrTaNb high-entropy alloy.* Materials Science and Engineering: A, 2016. **654**: p. 30-38.
8. Sahlberg, M., et al., *Superior hydrogen storage in high entropy alloys.* Sci Rep, 2016. **6**: p. 36770.
9. Zlotea, C., et al., *Hydrogen sorption in TiZrNbHfTa high entropy alloy.* Journal of Alloys and Compounds, 2019. **775**: p. 667-674.
10. Kirchheim, R., *Hydrogen solubility and diffusivity in defective and amorphous metals.* Progress in Materials Science, 1988. **32**(4): p. 261-325.
11. Pundt, A. and R. Kirchheim, *HYDROGEN IN METALS: Microstructural Aspects.* Annual Review of Materials Research, 2006. **36**(1): p. 555-608.
12. Hruška, P., et al., *Characterization of defects in titanium created by hydrogen charging.* International Journal of Hydrogen Energy, 2017. **42**(35): p. 22557-22563.
13. Braeckman, B.R. and D. Depla, *On the amorphous nature of sputtered thin film alloys.* Acta Materialia, 2016. **109**: p. 323-329.
14. Braeckman, B.R., et al., *High entropy alloy thin films deposited by magnetron sputtering of powder targets.* Thin Solid Films, 2015. **580**: p. 71-76.
15. Braeckman, B.R. and D. Depla, *Structure formation and properties of sputter deposited Nbx-CoCrCuFeNi high entropy alloy thin films.* Journal of Alloys and Compounds, 2015. **646**: p. 810-815.
16. Guo, S., et al., *More than entropy in high-entropy alloys: Forming solid solutions or amorphous phase.* Intermetallics, 2013. **41**: p. 96-103.
17. Tüten, N., et al., *Microstructure and tribological properties of TiTaHfNbZr high entropy alloy coatings deposited on Ti 6Al 4V substrates.* Intermetallics, 2019. **105**: p. 99-106.
18. Motallebzadeh, A., et al., *Mechanical Properties of TiTaHfNbZr High-Entropy Alloy Coatings Deposited on NiTi Shape Memory Alloy Substrates.* Metallurgical and Materials Transactions A, 2018. **49**(6): p. 1992-1997.
19. Kim, Y.S., et al., *Investigation of structure and mechanical properties of TiZrHfNiCuCo high entropy alloy thin films synthesized by magnetron sputtering.* Journal of Alloys and Compounds, 2019. **797**: p. 834-841.
20. Cropper, M.D., *Thin films of AlCrFeCoNiCu high-entropy alloy by pulsed laser deposition.* Applied Surface Science, 2018. **455**: p. 153-159.
21. Lukac, F., et al., *Spark plasma sintering of gas atomized high-entropy alloy HfNbTaTiZr.* Journal of Materials Research, 2018. **33**(19): p. 3247-3257.
22. Coelho, A.A., *TOPASandTOPAS-Academic: an optimization program integrating computer algebra and crystallographic objects written in C++.* Journal of Applied Crystallography, 2018. **51**(1): p. 210-218.
23. Yeh, J.J. and I. Lindau, *Atomic subshell photoionization cross sections and asymmetry parameters: $1 \leqslant Z \leqslant 103$.* Atomic Data and Nuclear Data Tables, 1985. **32**(1): p. 1-155.
24. Moulder, J.F., J. Chastain, and R.C. King, *Handbook of x-ray photoelectron spectroscopy: a reference book of standard spectra for identification and interpretation of XPS data*. 1995: Eden Prairie Minnesota : Physical Electronics.

25. Wagner, A., et al., *Positron annihilation lifetime and Doppler broadening spectroscopy at the ELBE facility* AIP Conference Proceedings, 2018. **1970**: p. 040003
26. Gabriel, F., et al., *The Rossendorf radiation source ELBE and its FEL projects.* Nuclear Instruments and Methods in Physics Research Section B: Beam Interactions with Materials and Atoms, 2000. **161-163**: p. 1143-1147.
27. Schultz, P.J. and K.G. Lynn, *Interaction of positron beams with surfaces, thin films, and interfaces.* Reviews of Modern Physics, 1988. **60**(3): p. 701-779.
28. Čížek, J., *PLRF Code for Decomposition of Positron Lifetime Spectra.* Acta Physica Polonica A, 2020. **137**(2): p. 177-187.
29. Lan, S., et al., *Structure origin of a transition of classic-to-avalanche nucleation in Zr-Cu-Al bulk metallic glasses.* Acta Materialia, 2018. **149**: p. 108-118.
30. Ma, D., A.D. Stoica, and X.L. Wang, *Power-law scaling and fractal nature of medium-range order in metallic glasses.* Nat Mater, 2009. **8**(1): p. 30-4.
31. Matsunami, N., et al., *Energy dependence of the ion-induced sputtering yields of monatomic solids.* Atomic Data and Nuclear Data Tables, 1984. **31**(1): p. 1-80.
32. Seah, M.P., et al., *An accurate semi-empirical equation for sputtering yields I: for argon ions.* Surface and Interface Analysis, 2005. **37**(5): p. 444-458.
33. NPL. *Sputter yield values*. 2020; Available from: https://www.npl.co.uk/research/mass-spectrometry/secondary-ion/sputter-yield-values.
34. Powell, C.J., *Recommended Auger parameters for 42 elemental solids.* Journal of Electron Spectroscopy and Related Phenomena, 2012. **185**(1-2): p. 1-3.
35. Campbell, J.L. and T. Papp, *Widths of the Atomic K–N7 Levels.* Atomic Data and Nuclear Data Tables, 2001. **77**(1): p. 1-56.
36. Biesinger, M.C. *X-ray Photoelectron Spectroscopy (XPS) Reference Pages*. 2020; Available from: http://www.xpsfitting.com.
37. Jayaraj, J., et al., *Corrosion behavior and surface film characterization of TaNbHfZrTi high entropy alloy in aggressive nitric acid medium.* Intermetallics, 2017. **89**: p. 123-132.
38. Morant, C., L. Galán, and J.M. Sanz, *An XPS study of the initial stages of oxidation of hafnium.* Surface and Interface Analysis, 1990. **16**(1-12): p. 304-308.
39. Bespalov, I., et al., *Initial stages of oxide formation on the Zr surface at low oxygen pressure: An in situ FIM and XPS study.* Ultramicroscopy, 2015. **159 Pt 2**: p. 147-51.
40. Ma, W., et al., *Non-equilibrium oxidation states of zirconium during early stages of metal oxidation.* Applied Physics Letters, 2015. **106**(10).
41. Greenwood, N.N. and A. Earnshaw, *Chemistry of the Elements*. 2nd ed. 1997: Elsevier. 1600.
42. Schweitzer, P.A., *Metallic materials: Physical, Mechanical, and Corrosion Properties*. 2003, New York: Marcel Dekker, Inc.
43. Backman, L. and E.J. Opila, *Thermodynamic assessment of the group IV, V and VI oxides for the design of oxidation resistant multi-principal component materials.* Journal of the European Ceramic Society, 2019. **39**(5): p. 1796-1802.
44. Backman, L., et al., *Part I: Theoretical predictions of preferential oxidation in refractory high entropy materials.* Acta Materialia, 2020. **197**: p. 20-27.
45. Backman, L., et al., *Part II: Experimental verification of computationally predicted preferential oxidation of refractory high entropy ultra-high temperature ceramics.* Acta Materialia, 2020. **197**: p. 81-90.

46. Watts, J.F. and J. Wolstenholme, *An Introduction to Surface Analysis by XPS and AES*. 2019: Wiley.
47. Lukáč, F., et al., *Defects in Thin Layers of High Entropy Alloy HfNbTaTiZr.* Acta Physica Polonica A, 2020. **137**(2): p. 219-221.
48. Lukáč, F., et al., *Defects in High Entropy Alloy HfNbTaTiZr Prepared by High Pressure Torsion.* Acta Physica Polonica A, 2018. **134**(3): p. 891-894.
49. Čížek, J., et al., *Strength enhancement of high entropy alloy HfNbTaTiZr by severe plastic deformation.* Journal of Alloys and Compounds, 2018. **768**: p. 924-937.
50. Kuriplach, J., et al., *Behavior of Positrons in the HfNbTaTiZr Complex Concentrated Alloy.* Acta Physica Polonica A, 2020. **137**(2): p. 260-265.

- Amorphous HfNbTaTiZr high entropy alloy thin films were deposited by DC magnetron sputtering.
- A fine structure of round-shaped amorphous clusters ~10 nm was observed.
- Oxidation at ambient atmosphere leads to a preferential formation of Ti-, Hf- and Zr- oxide nanoclusters.
- Oxidation takes place predominantly in large open volumes in between cluster aggregates.

Figure 1a

Click here to access/download;Figure;Fig_TEMimg_HEAM1_PH.jpg

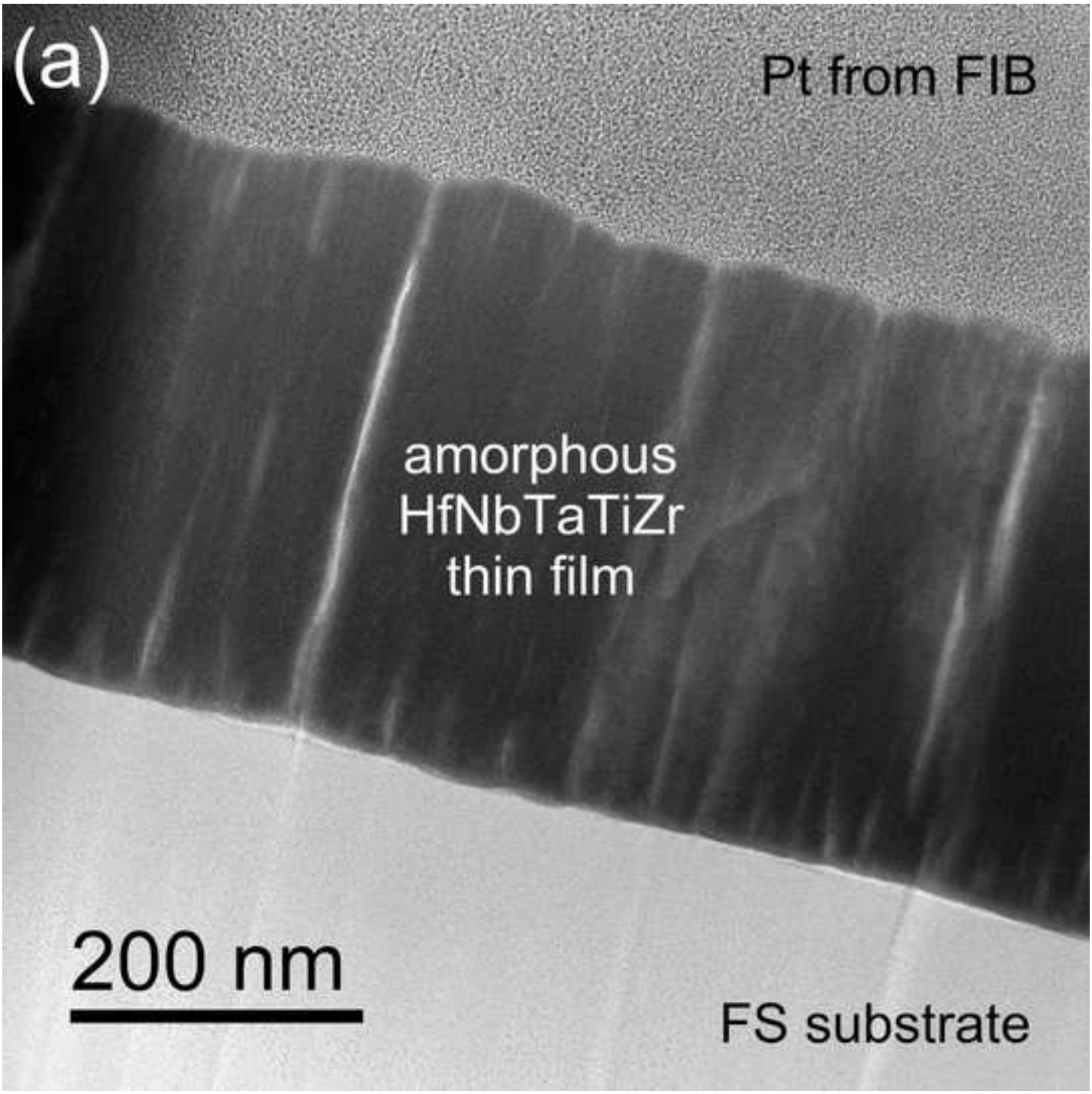

Figure 1b

Click here to access/download;Figure;Fig_HRTEM_HEAM1_PH.jpg

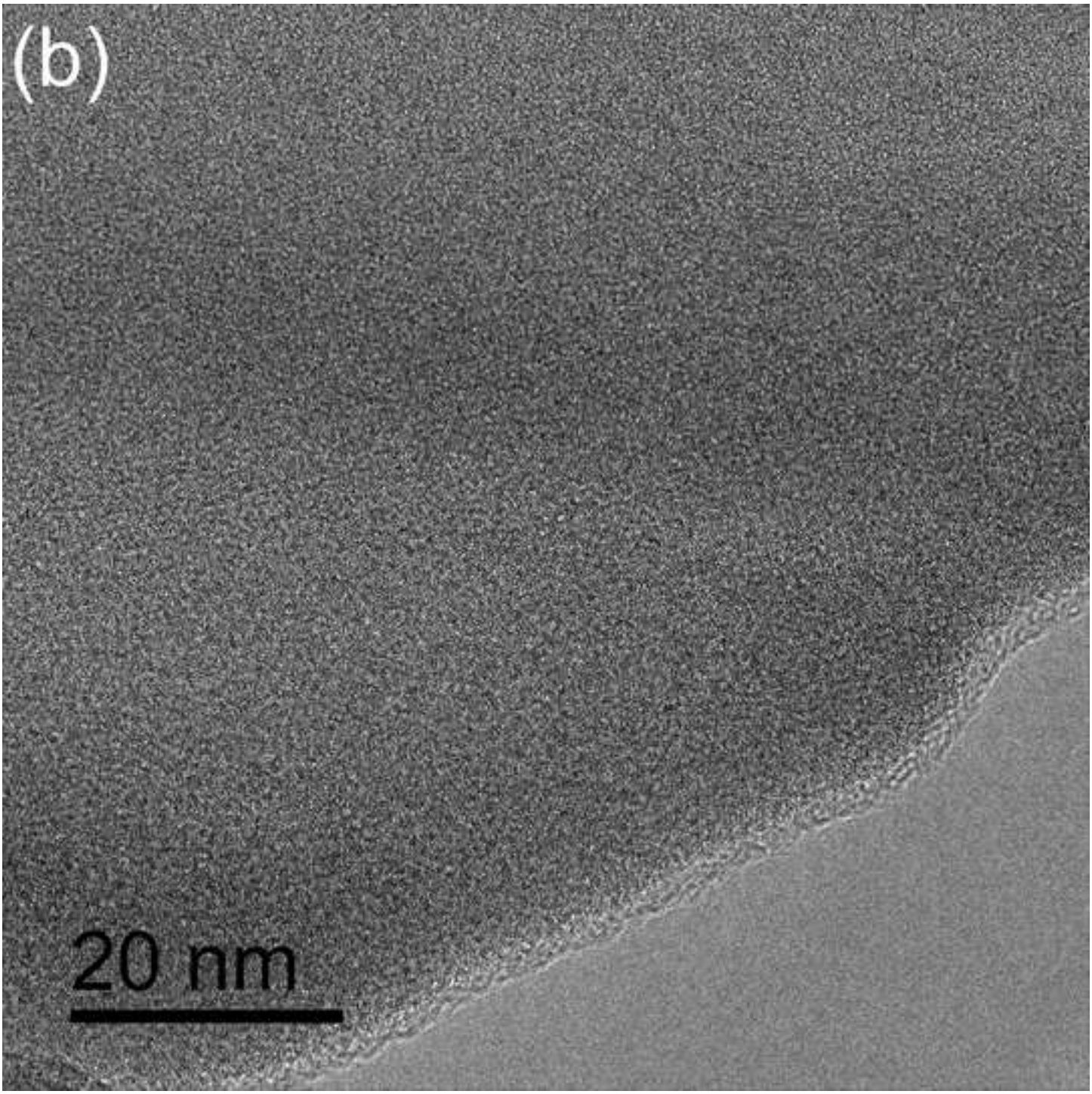

Figure 1c

Click here to access/download;Figure;Fig_TEMdiff_HEAM1_PH.jpg

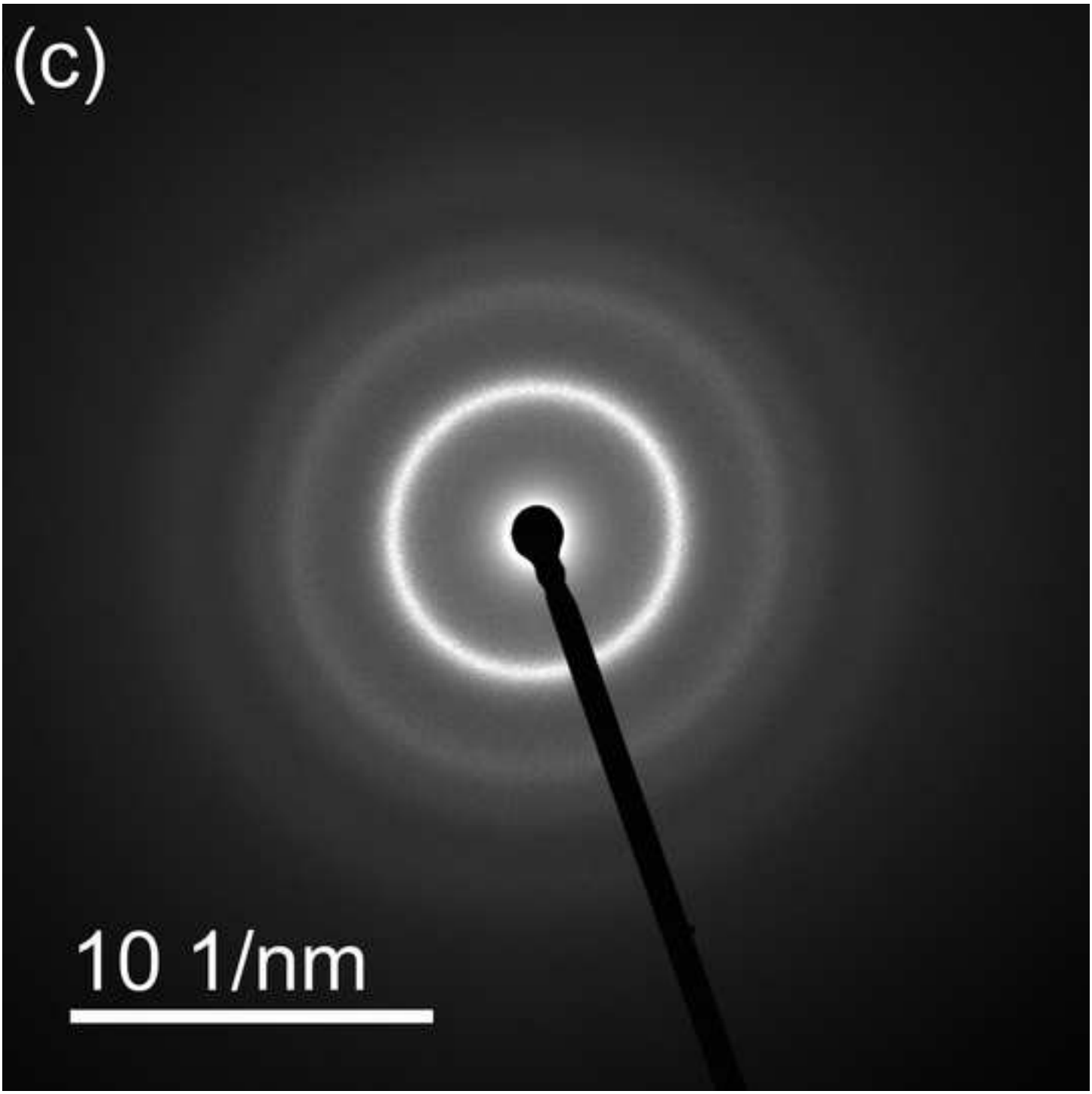

Figure 2

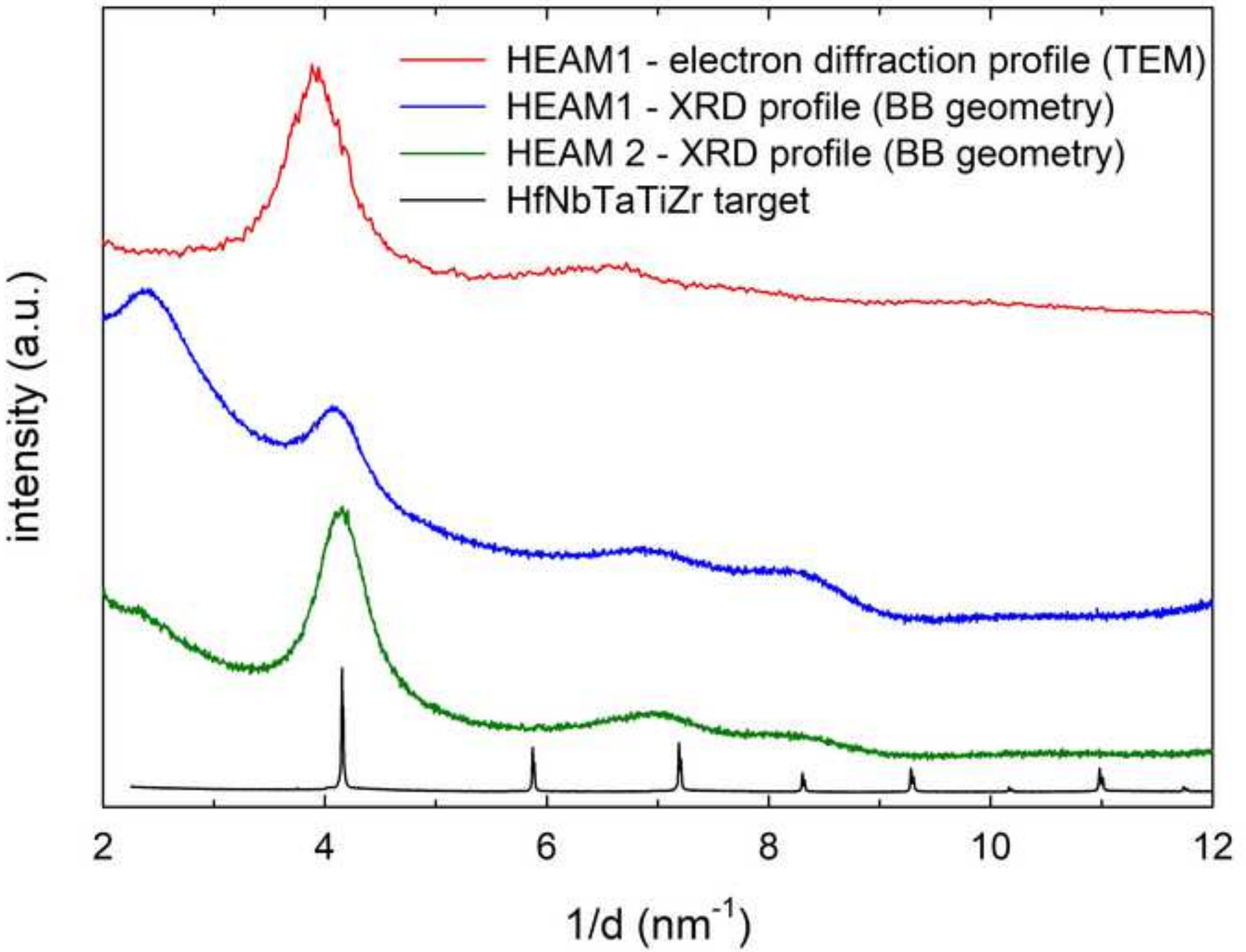

Figure 3a

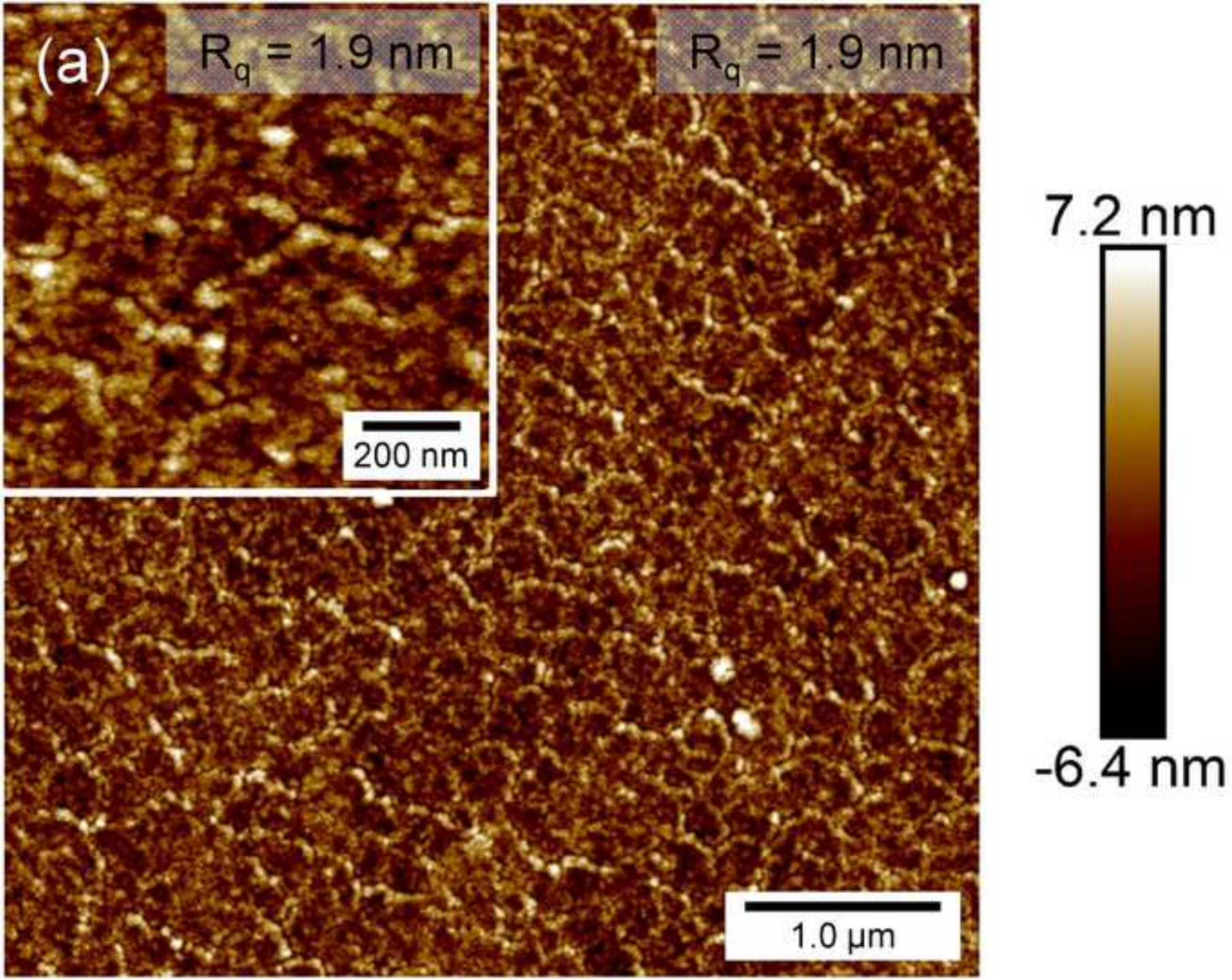

Figure 3b

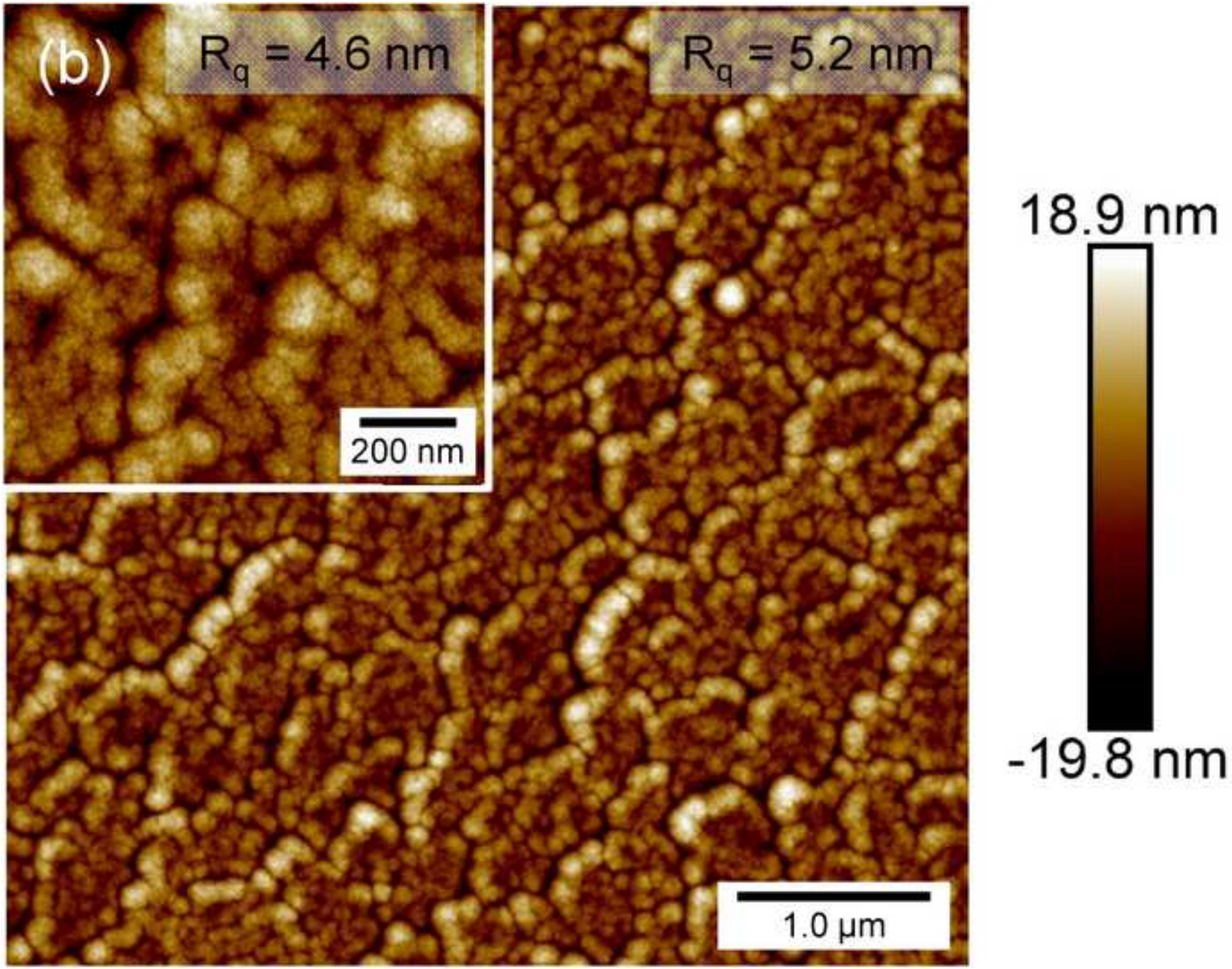

Figure 4a

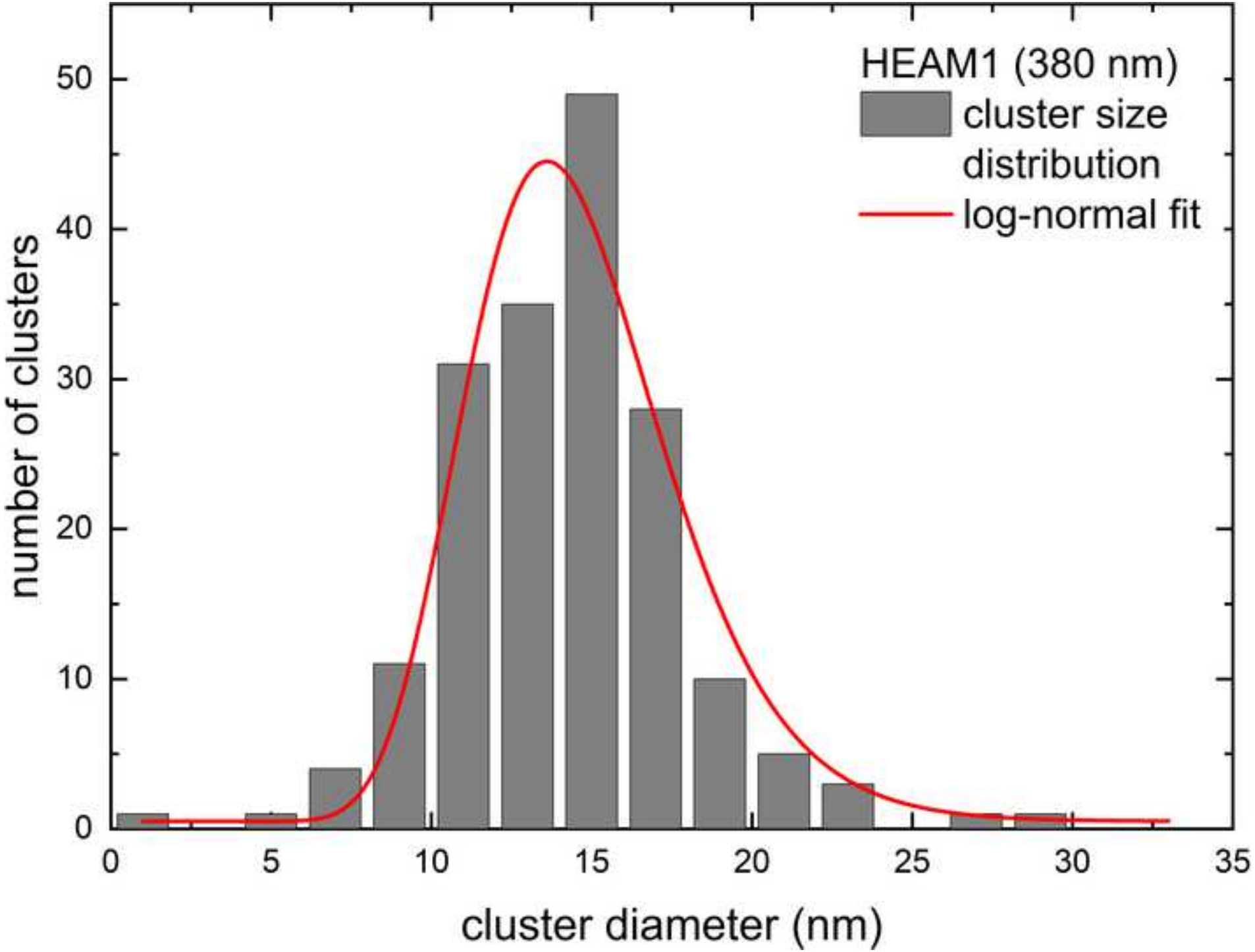

Figure 4b

Click here to access/download;Figure;HEAM2 grain distribution new2.jpg

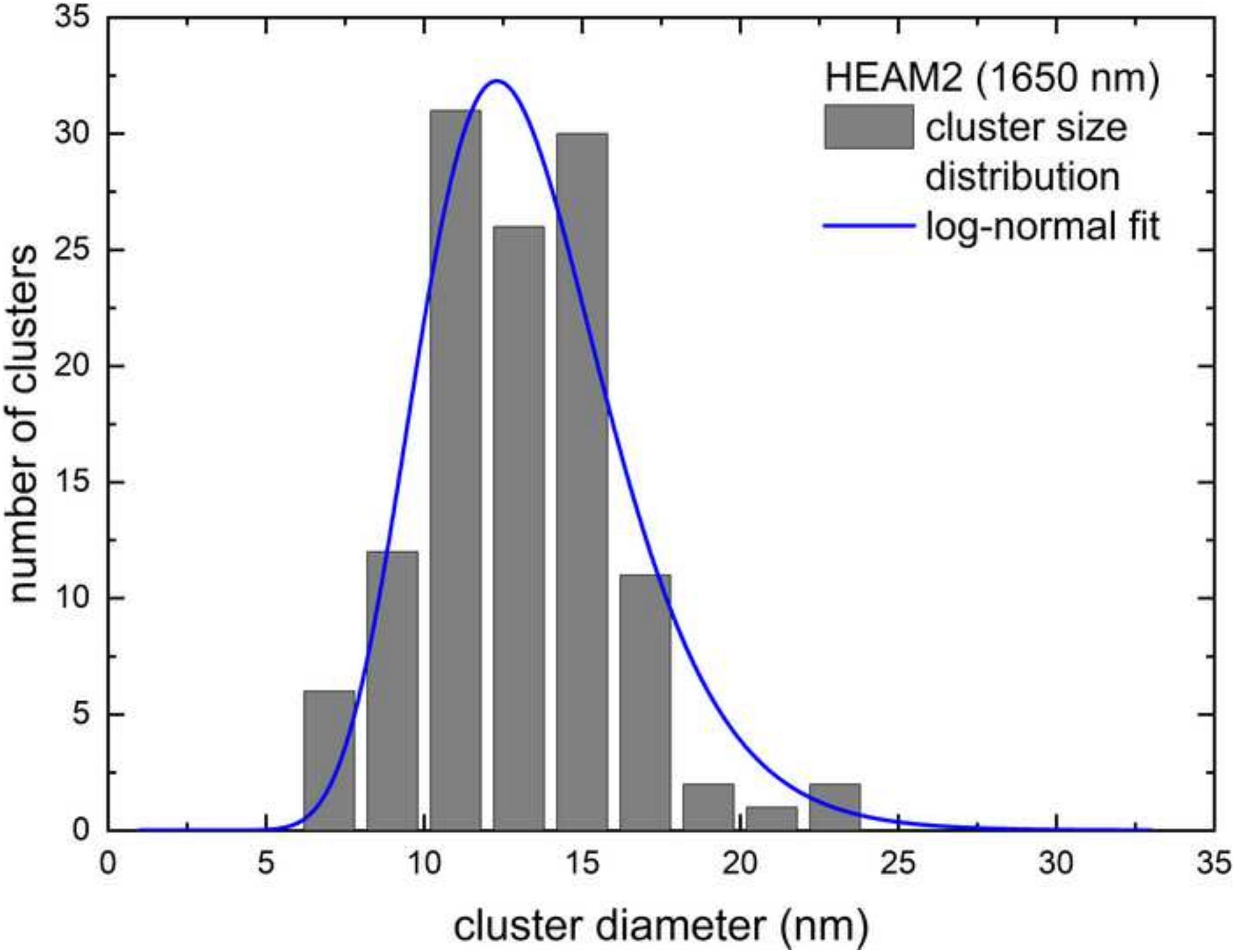

Figure 5

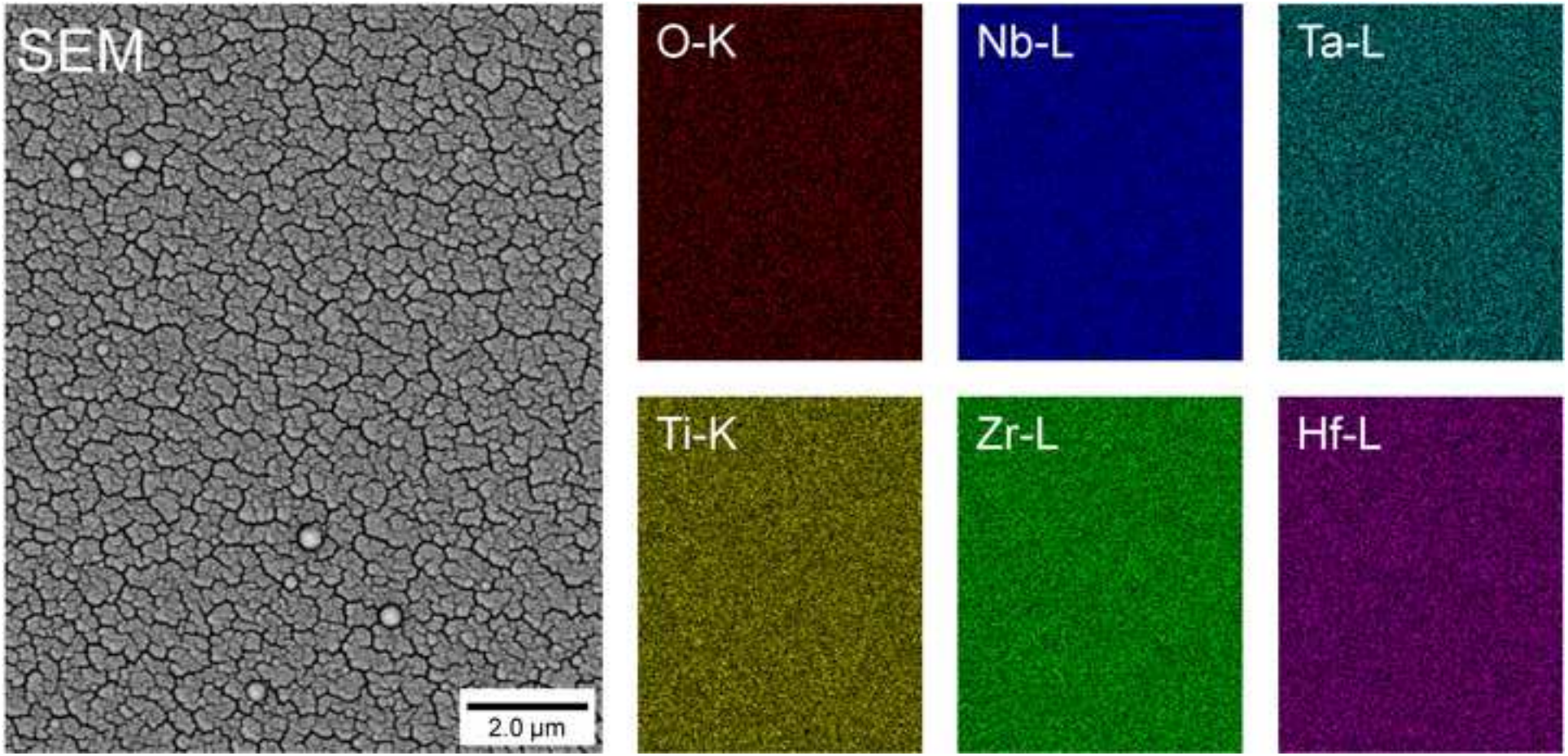

Figure 6

Click here to access/download;Figure;XPS HEAM Corel3.png

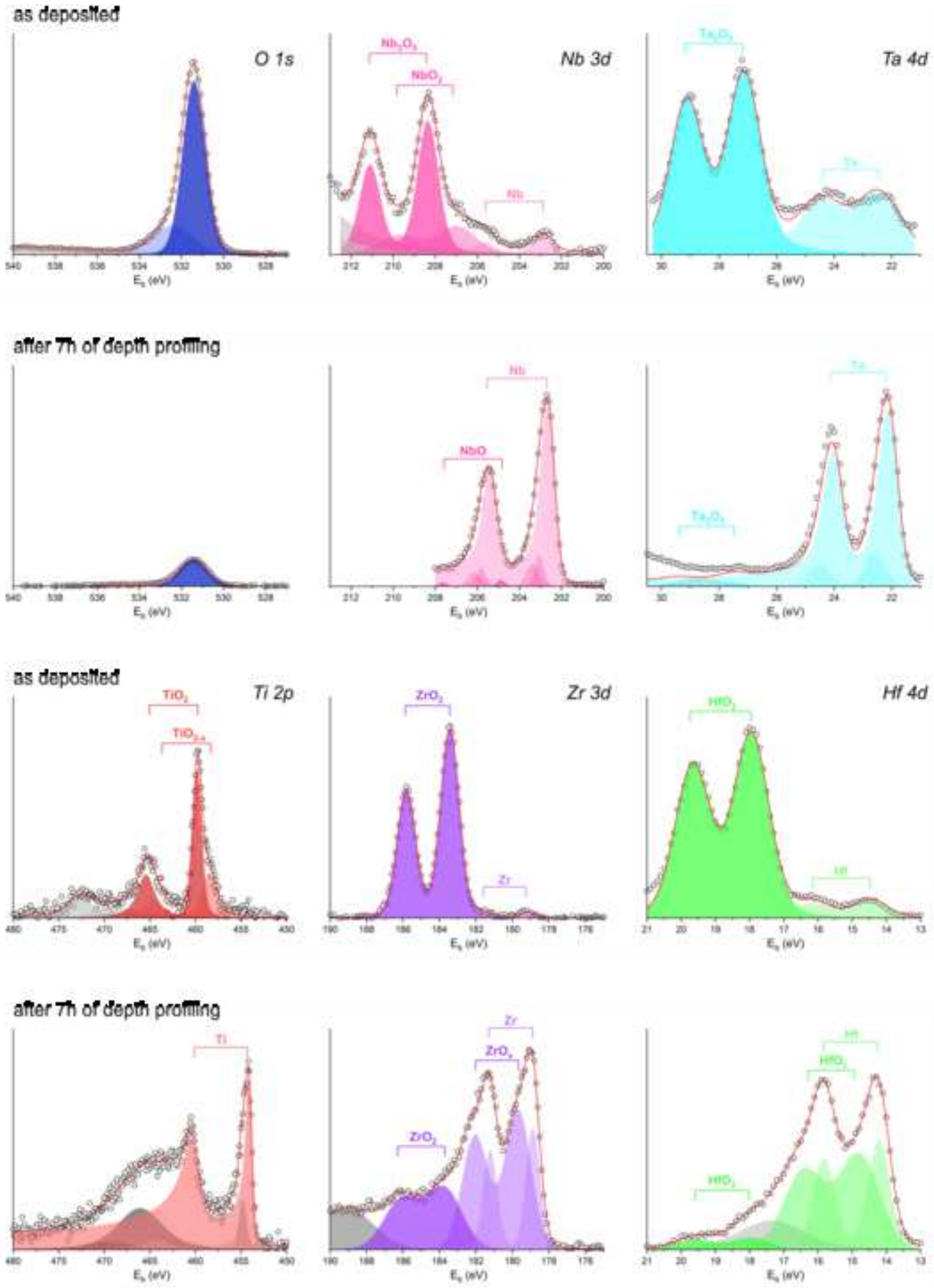

Figure 7a

Click here to access/download;Figure;mean-lifetime-narrow2.JPG

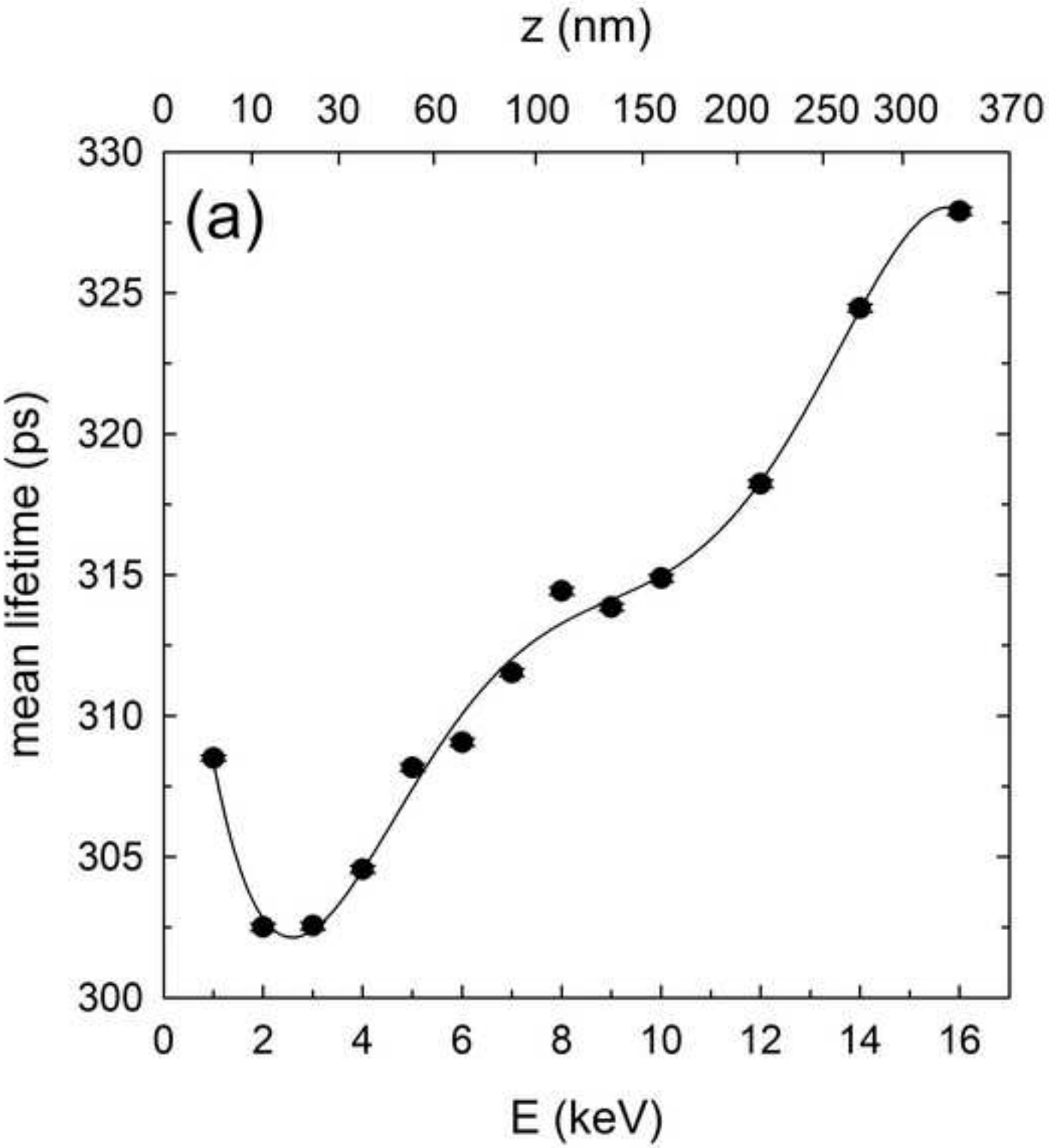

Figure 7b

Click here to access/download;Figure;lifetimes-narrow2.JPG

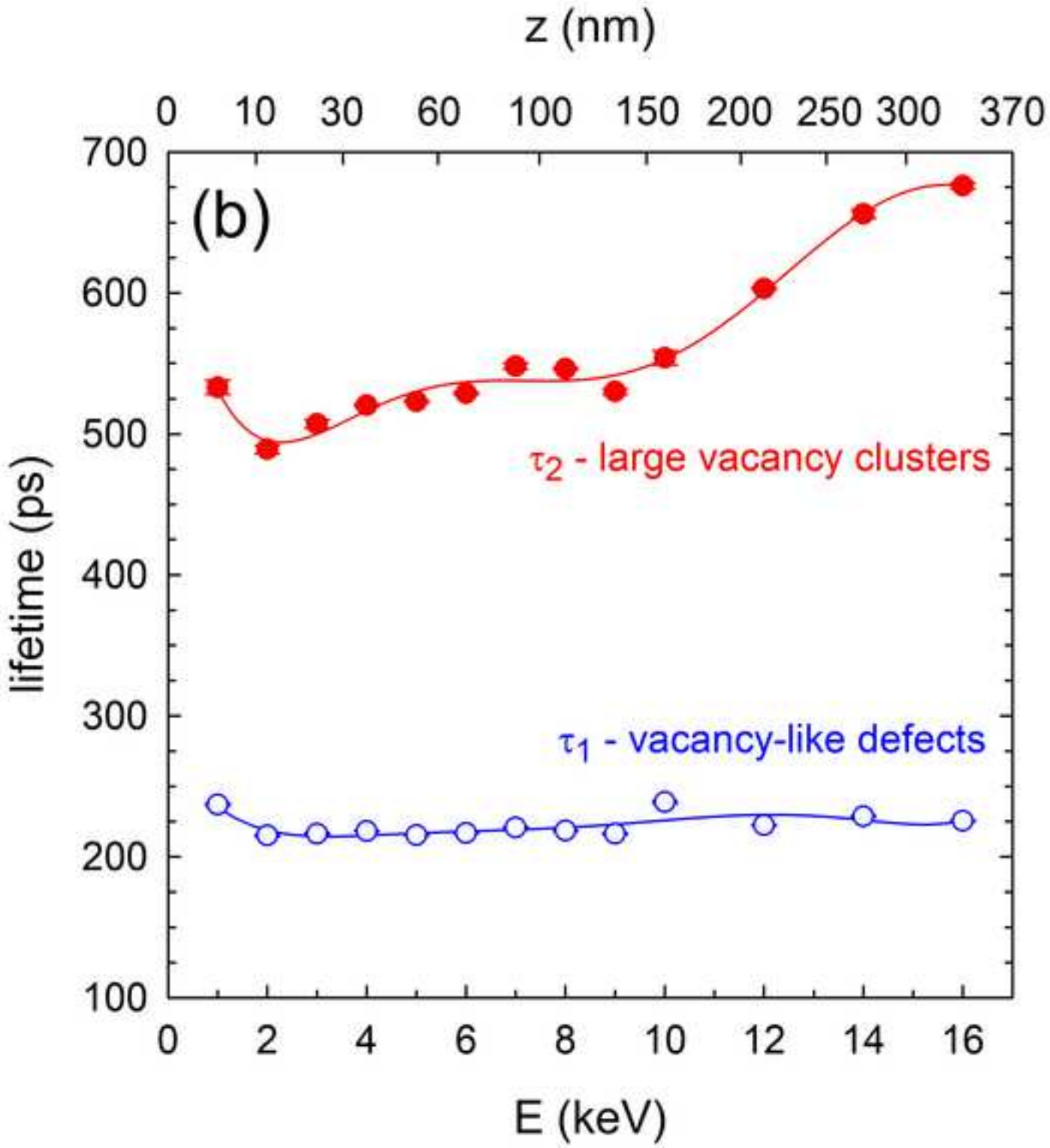

Figure 7c

Click here to access/download;Figure;intensities-narrow2.JPG

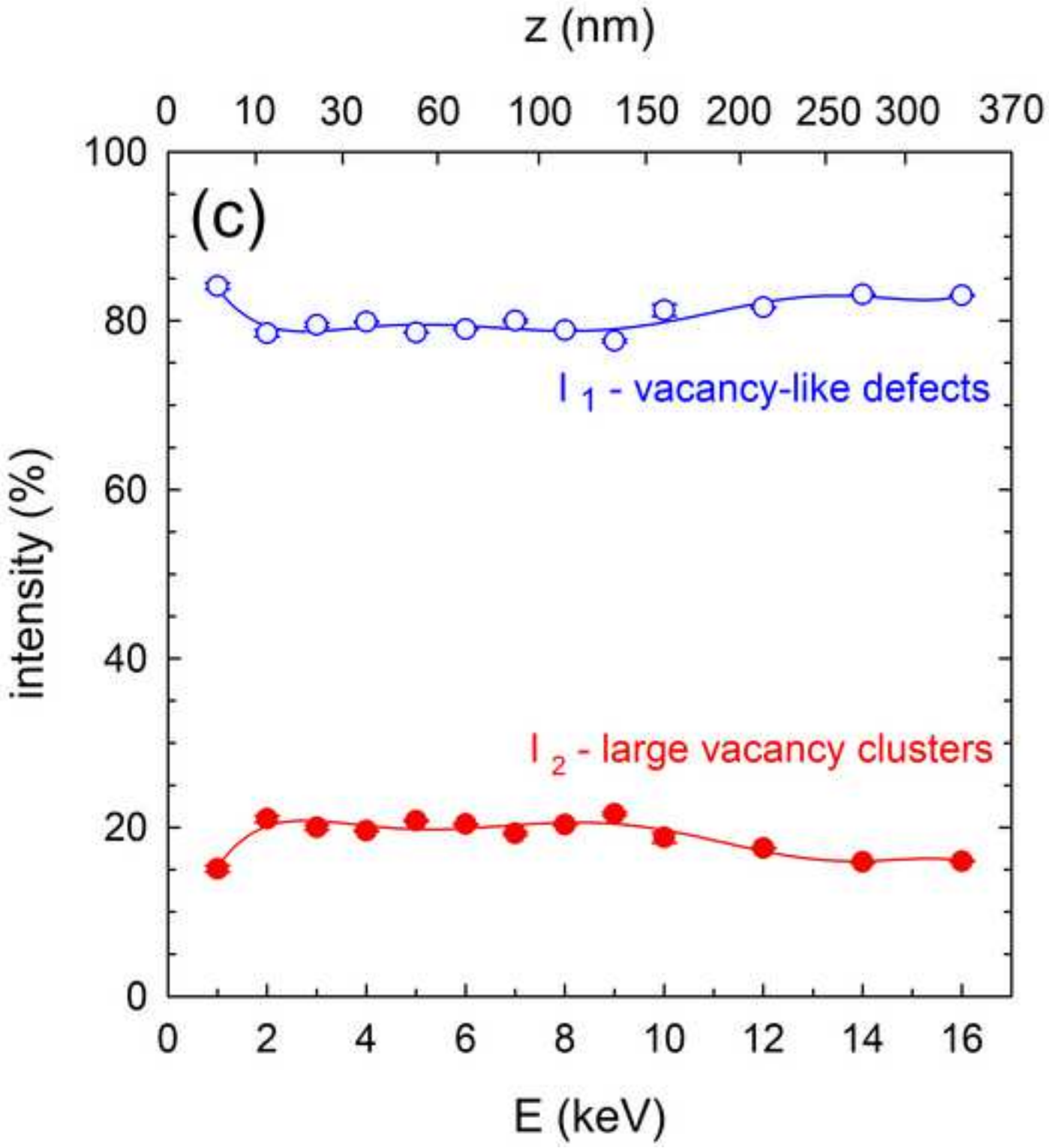

CRediT author statement

Petr Hruška: Conceptualization, Validation, Formal Analysis, Investigation, Writing – Original Draft
František Lukáč: Conceptualization, Formal Analysis, Investigation, Resources, Writing - Review & Editing, Visualization
Stanislav Cichoň: Formal Analysis, Investigation, Writing - Review & Editing
Martin Vondráček: Formal Analysis, Investigation, Writing - Review & Editing
Jakub Čížek: Conceptualization, Formal Analysis, Investigation, Funding Acquisition, Writing - Review & Editing
Ladislav Fekete: Formal Analysis, Investigation
Ján Lančok: Conceptualization, Resources, Funding Acquisition
Jozef Veselý: Investigation
Peter Minárik: Investigation
Miroslav Cieslar: Resources
Oksana Melikhova: Investigation
Tomáš Kmječ: Formal Analysis, Investigation
Maciej Oskar Liedke: Investigation
Maik Butterling: Software, Investigation
Andreas Wagner: Investigation, Resources

*Declaration of Interest Statement

Declaration of interests

☒ The authors declare that they have no known competing financial interests or personal relationships that could have appeared to influence the work reported in this paper.

☐The authors declare the following financial interests/personal relationships which may be considered as potential competing interests:

Oxidation of amorphous HfNbTaTiZr high entropy alloy thin films prepared by DC magnetron sputtering

Petr Hruška[1,2,*], František Lukáč[1,3], Stanislav Cichoň[2], Martin Vondráček[2], Jakub Čížek[1], Ladislav Fekete[2], Ján Lančok[2], Jozef Veselý[1], Peter Minárik[1], Miroslav Cieslar[1], Oksana Melikhova[1], Tomáš Kmječ[1], Maciej Oskar Liedke[4], Maik Butterling[4], and Andreas Wagner[4]

[1] Charles University, Faculty of Mathematics and Physics, V Holešovičkách 2, 180 00 Prague, Czech Republic
[2] Institute of Physics of the Czech Academy of Sciences, Na Slovance 2, 182 21, Prague, Czech Republic
[3] Institute of Plasma Physics of the Czech Academy of Sciences, Za Slovankou 3, 182 00, Prague, Czech Republic
[4] Helmholtz-Zentrum Dresden-Rossendorf, Institute of Radiation Physics, Bautzner Landstrasse 400, 01328 Dresden, Germany

*corresponding author: hruskap@fzu.cz

Keywords: high entropy alloys, HfNbTaTiZr, magnetron sputtering, X-ray photoelectron spectroscopy, positron annihilation spectroscopy

Abstract

High entropy alloys represent a new type of materials with a unique combination of physical properties originating from the occurrence of single-phase solid solutions of numerous elements. The preparation of nanostructured or amorphous structure in a form of thin films promises increased effective surface and high intergranular diffusion of elements as well as a high affinity to oxidation. In this work, we studied HfNbTaTiZr thin films, deposited at room temperature by DC magnetron sputtering from a single bcc phase target. Films exhibit cellular structure (~100 nm) with fine substructure (~10 nm) made of round-shape amorphous clusters. The composition is close to equimolar with slight Ti enrichment and without any mutual segregation of elements. Oxidation at the ambient atmosphere leads to the formation of Ti, Zr, Nb, Hf, and Ta oxide clusters in the film up to the depth of 200 – 350 nm out of the total film thickness of 1650 nm. Oxygen absorption takes place preferentially in the large vacancy clusters located in between the amorphous cluster aggregates. The dominant type of defect are small open volumes with a size comparable with vacancy. The distribution of these defects is uniform with depth and is not influenced by the presence of oxygen in the film.

1. Introduction

High entropy alloys (HEA) called also complex concentrated alloys or multi-principal element alloys [1] are a group of materials with a combination of interesting properties [2-4]. While most conventional alloys are based on one principal matrix element with alloying elements of

lower concentration, these alloys are a mixture of at least four elements in a similar atomic ratio. The high configurational entropy of this system causes the formation of a single solid solution phase at high temperatures [5]. A high number of elements promises a combination of interesting phases [6, 7] and intriguing deformation behavior [8] when annealed. Therefore, new combinations of physical properties are expected, namely mechanical [2, 3], oxidation [9], irradiation [10], and wear resistance [11].

HfNbTaTiZr alloy belongs to a group of refractory materials with a high melting point and thermal stability [9] with enhanced ductility and strength [12]. The casting of this alloy results in dendritic structure and subsequent homogenization annealing produces large grains and the alloy is susceptible to embrittlement from absorbed atmosphere impurities [13]. Moreover, local variations of the lattice parameter lead to the distribution of sizes of interstitials [1] forming an open structure favorable for hydrogen absorption. Interaction of refractory high entropy alloys with hydrogen has been widely studied [14, 15].

For hydrogen absorption in metals, a large surface area together with small grains microstructure is advantageous for diffusion along grain boundaries into the material [16-18]. A nanocrystalline microstructure can be achieved by annealing of the amorphous phase. Amorphous HEA, often called metallic glasses (MG) have strong topological and chemical disorder and may have special properties different from bulk MG or HEA [4]. They can be prepared either by a high quenching rate of liquid phase [19] or by various deposition techniques [20]. It was found that the composition driven effects in sputtered thin films are decisive about the amorphization of the alloys, and the more complex is the composition of the alloy, the higher is the occurrence of amorphous content [21, 22]. A mechanism of phase selection in high entropy alloys between solid solution and amorphous phase was proposed based on atomic size dispersion and mixing enthalpy [19]. Therefore, it is interesting to prepare an amorphous phase from an alloy typical for single solution formation. Moreover, the hardness of such an amorphous thin film is much higher than bulk material [23]. Oxidation of amorphous or nanocrystalline film may block effective hydrogen absorption in the film though.

Two HfNbTaTiZr thin films with different thicknesses were prepared by DC magnetron sputtering. The deposition at room temperature is favorable for the formation of a nanocrystalline to an amorphous structure [24]. The effect of various deposition conditions (deposition rate, substrate temperature) and film composition to the structure of thin films prepared by magnetron sputtering was studied e.g. in [21, 25]. Oxidation of HEA films can be well studied by X-ray photoelectron spectroscopy combined with depth profiling [26]. Positron annihilation lifetime spectroscopy is a versatile tool providing information about open volumes, important for oxidation and hydrogen absorption properties, in both crystalline and amorphous structures.

2. Experimental

HEA films were prepared by DC magnetron sputtering in an ultra-high vacuum (UHV) deposition chamber. A DC power supply was operated at the power of 10 W, the voltage and current lied in the range of 260 V – 200 V and 38 – 49 mA respectively resulting in a relatively slow deposition rate of approximately 6 nm/min. The base pressure in the UHV chamber of 10^{-7} – 10^{-8} Pa was ensured by a turbomolecular and an ion pump. The magnetron discharge was maintained in the Ar atmosphere at a constant pressure of 2 Pa, which was regulated by a needle valve, the Ar flow was fixed at 14 sccm. A single-phase round shape HfNbTaTiZr target with 1-inch diameter prepared by spark plasma sintering (SPS) from a gas atomized powder of HfNbTaTiZr alloy [27] was used as a sputtering target. The SPS processing of the target was performed at 1300°C for 2 min using a pressure of 100 MPa. The target exhibited a single bcc phase with the equiatomic composition, as confirmed by X-ray diffraction (XRD) and X-ray fluorescence (XRF), respectively.

HEA films were deposited on amorphous fused silica (FS) substrates with dimensions 10 × 10 mm^2, which were kept at room temperature (RT). The target to substrate distance was fixed at 100 mm. Samples with 2 different thicknesses, determined by transmission electron microscopy (TEM), were studied: (i) HEAM1 – 380 nm “thin” film and (ii) HEAM2 – 1650 nm “thick” film.

X-ray diffraction (XRD) analysis was carried out using Cu-Kα radiation on a Bruker Discover diffractometer equipped with a 1D LynxEye. XRD measurements were performed in the Bragg-Brentano symmetrical geometry at 2θ angles from 10° to 140°. The TOPAS V5 code [28] was employed for the Rietveld refinement analysis of XRD spectra.

Lamellas for TEM investigation were prepared by a focused ion beam (FIB) in a scanning electron microscope (SEM) ZEISS Auriga Compact using Ga^+ ions. A platinum layer was deposited for the protection of the investigated layer before the preparation of the lamellas. The final Ga^+ ion-polishing of the lamellas was performed by FIB with acceleration voltage decreased down to 2 kV. TEM observations were performed on JEOL 2200FS operating at 200 kV. FEI Quanta 200F SEM equipped with an Energy-dispersive X-ray spectroscope (EDS) was employed for the mapping of chemical elements.

Atomic force microscopy (AFM) was employed to characterize the films’ surface morphology. AFM measurements were carried out at room temperature on an ambient AFM (Bruker, Dimension Icon) in Peak Force Tapping mode with ScanAsyst Air tips (Bruker, k = 0.4 N/m, nominal tip radius 2 nm). Measured topographies have 512 × 512 points resolution.

The films’ composition was investigated using XRF spectrometer Eagle III µProbe with a beam of 300 µm diameter.

X-ray Photoelectron Spectroscopy (XPS) analysis was performed in the Omicron NanoESCA instrument using a monochromatized Al-Kα radiation source (E = 1486.7 eV). Under these conditions, the information depth is a few nanometers. Elemental composition was calculated from peak areas employing photo-emission cross-section [29, 30]. For analysis of subsurface

regions, depth profiling of the samples was enabled by an Ar^+ ion sputter gun in the preparation chamber of the NanoESCA instrument with the sputtering conditions E = 3 keV, pressure 2×10^{-4} Pa and normal incidence angle.

Positron annihilation lifetime spectroscopy (PALS) was carried out on a pulsed slow positron beam MePS [31] operating at the ELBE (Electron LINAC with high Brilliance and low Emittance) facility [32] in the Helmholtz-Zentrum Dresden-Rossendorf. The energy of incident positrons in the beam was varied in the range from 1 to 16 keV, which corresponds to the mean positron implantation depth into HfNbTaTiZr ranging from 4 to 340 nm as calculated using the Makhovian implantation profile [33] and the theoretical bulk density of 10 g/cm^3 for the HfNbTaTiZr alloy [5]. Positron lifetime spectra were collected using a digital spectrometer [31] with a time resolution of 250 ps (FWHM of the resolution function). The decomposition of positron lifetime spectra into individual exponential components was performed using the PLRF code [34].

3. Results and discussion

3.1. Amorphous structure

The microstructure of films can be inspected in detail by TEM observations of cross-sections of the film lamellas cut by FIB. Figure 1a shows a TEM image of a cross-section of the HEAM1 film. The high-resolution image of the film layer in Figure 1b shows that no crystalline structure is present in the film. Indeed, the electron diffraction pattern from the region of the whole cross-section of the 380 nm thick film HEAM1 in Figure 1c proves that there is neither a crystalline phase nor a preferred orientation of nanocrystalline grains. The electron diffraction pattern exhibits a broad intensive ring surrounded by a diffusive halo. This is a typical pattern for amorphous structure. The amorphous structure of the HEA films deposited on FS at RT was confirmed also by XRD measurements.

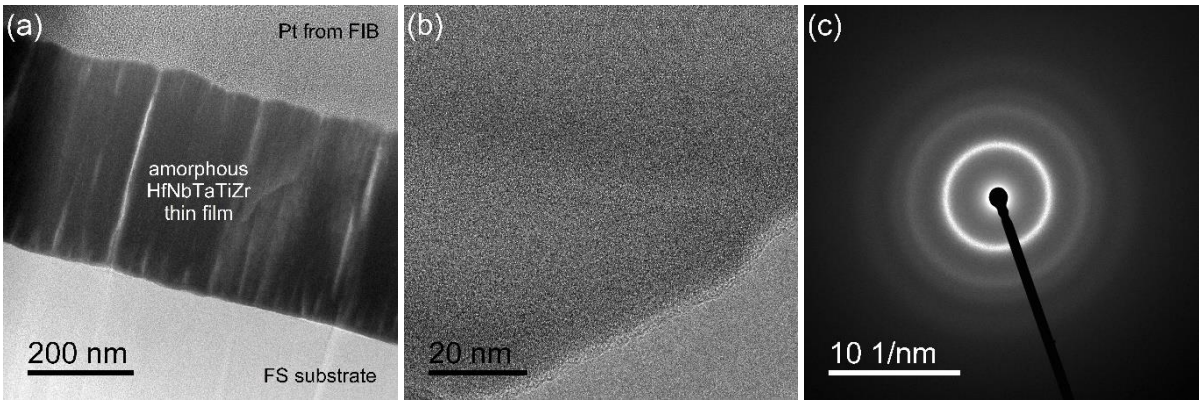

Figure 1: TEM measurements of the amorphous 380 nm thick HEAM1 film: (a) cross-section of the FIB cut lamella, (b) high-resolution TEM image of the HEA film layer, (c) electron diffraction pattern taken from the HEA film region.

Figure 2 compares XRD data measured in the symmetrical Bragg-Brentano geometry for HEAM1 and HEAM2 films and the electron diffraction pattern determined by TEM, i.e. radial profile of intensities from Figure 1c. The XRD pattern measured in the polycrystalline HfNbTaTiZr target is plotted in the figure as well for comparison. Single bcc structure with the lattice parameter a = 3.40835(2) Å agrees well with one of the authors' previous study [27]. The XRD patterns for both HEA films, HEAM1 and HEAM2, are similar to each other and are similar also to the electron diffraction pattern of HEAM1 measured by TEM, but clearly miss numerous reflections of the bcc phase present in the polycrystalline HfNbTaTiZr target. This effect cannot be due to the preferentially orientated growth of the HEA films, since the electron diffraction pattern in figure 1c shows no sign of texture in the circular pattern. Both X-ray and electron diffraction profiles are similar to a typical diffractogram of bulk metallic glasses, e.g. Zr-Cu-Al [35]. The first sharp diffraction peak, typical for metallic glasses, can be solely analyzed using peak broadening from the width of the Lorentzian curve and the coherence length can be calculated as 1.7(3) nm. Such value corresponds to the medium-range order in metallic glasses [36]. The amorphous diffusive halo at higher values of the scattering vector is split into few broad peaks visible in figures 1c and 2. Note that despite both X-ray and electron diffraction patterns look much alike, they are sensitive to different types of crystallographic planes, namely planes parallel with the substrate and planes perpendicular to the substrate for the XRD and TEM measurement, respectively. The similarity of the diffraction patterns measured by XRD and TEM, therefore, testifies that there is no preferential orientation of neither clusters nor cluster agglomerates, as observed by AFM, to the substrate in the HEA films.

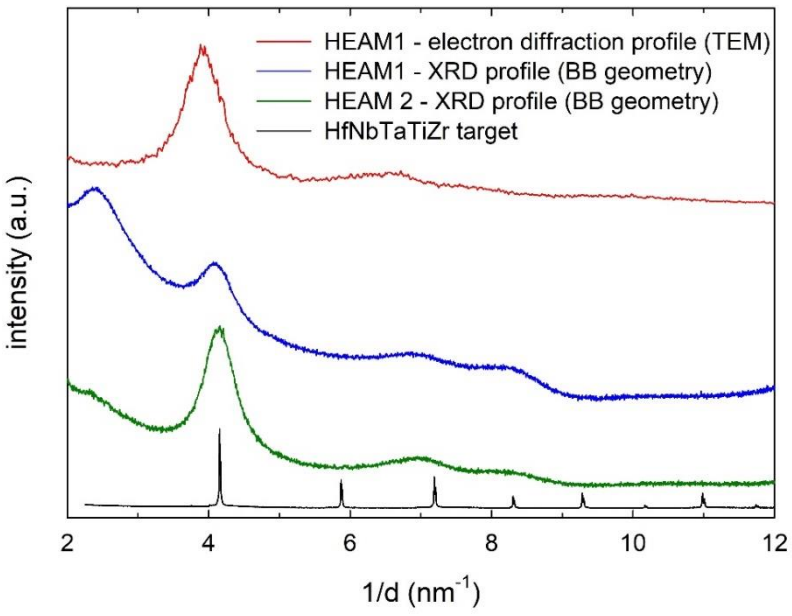

Figure 2: Comparison of the electron diffraction radial profile of the HEAM1 film and XRD profiles of HEAM1 and HEAM2 films measured in the symmetrical Bragg-Brentano (BB) geometry. XRD profile of the HfNbTaTiZr target prepared by SPS is included for comparison.

Figures 3a and 3b show AFM scans (area 5 × 5 μm^2) characterizing the morphology of the HEAM1 (thickness 380 nm) and HEAM2 (thickness 1650 nm) films. Details in higher magnification (area 1 × 1 μm^2) are shown in the insets. The RMS roughness R_q is listed in the top right corner of each scan. Note that R_q determined from larger scans is more accurate, since it is less affected by local deviations. Both films exhibit a very smooth surface which is a consequence of the slow deposition rate favoring smooth (atomic) layer-by-layer film growth. The roughness of the thicker film HEAM2 is 2-3 times higher compared to the thinner film HEAM1 while the thickness of the HEAM2 is more than 4 times higher than that of the HEAM1 film.

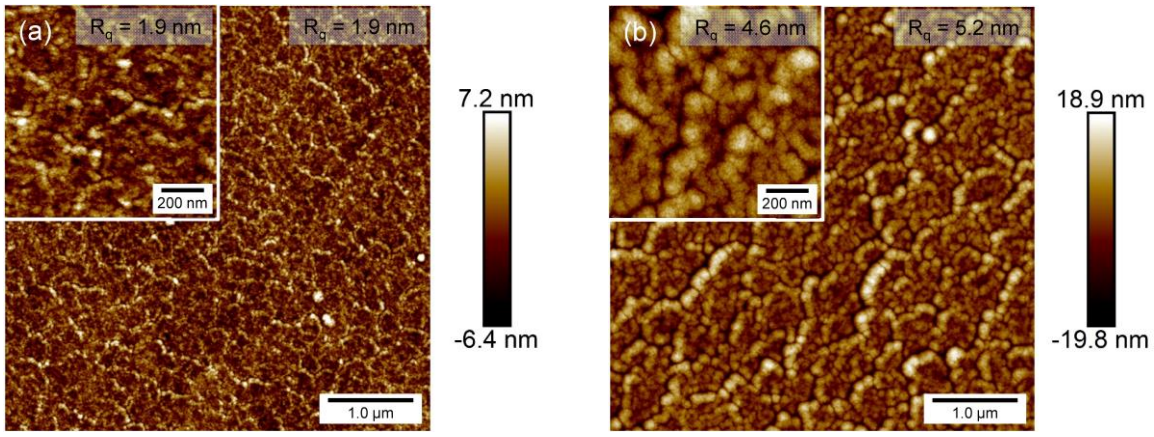

Figure 3: AFM measurement of (a) HEAM1 and (b) HEAM2 film, 5 × 5 μm^2 scans with 1 × 1 μm^2 detail. The surface roughness R_q is shown in each figure.

One can see in Figure 3 that the morphology of both films is very similar. The structure of HEAM2 film is more developed, as reflected by increased roughness, and consists of large aggregates, approx. 100 to 200 nm in size, separated by deep pits (dark regions in AFM scans). The aggregates consist of fine substructure with round-shape amorphous clusters, approx. 10 nm in size, see the inset in Figure 3b.

To investigate the fine substructure in detail, smaller scans containing 100 to 200 clusters were measured. Boundaries of clusters were manually identified and a surface area was evaluated for each region with a closed border. Using a round cluster approximation, cluster diameters were calculated. Histograms of cluster diameters for both films are shown in Figure 4 and can be reasonably approximated by the log-normal distribution. The mean cluster sizes for the HEAM1 and HEAM2 films were estimated to 14 nm and 12 nm respectively. Standard

deviations given by FWHMs of log-normal distributions are 7 nm for both films. Therefore we can say that the aggregate structure develops with the film thickness, as reflected by increasing roughness, while the aggregate substructure virtually remains the same independently on the film thickness.

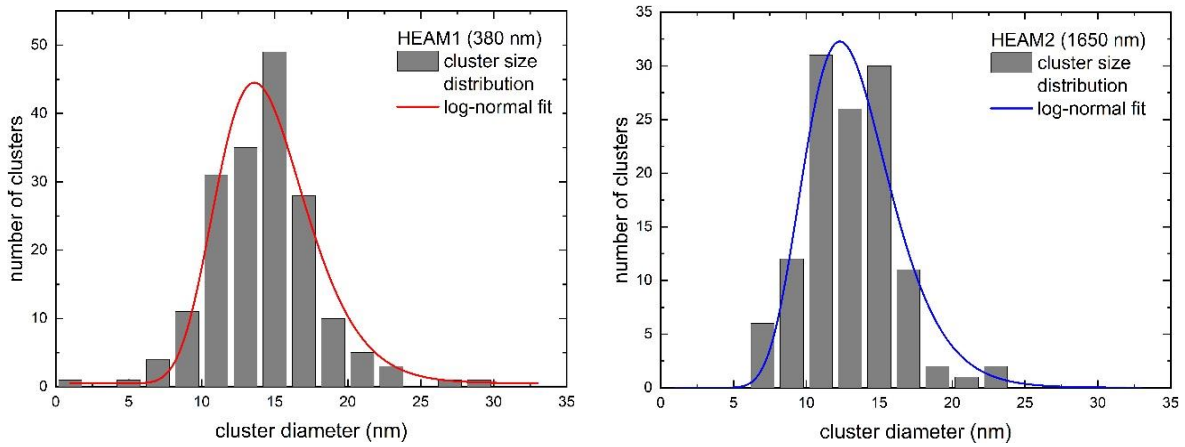

Figure 4: Histograms of cluster diameters for HEAM1 and HEAM2 films approximated by the log-normal distribution.

3.2. Oxidation of amorphous films

EDS analysis showed high oxygen content significantly exceeding the possible contribution of the FS (SiO_2) substrate. Considering the fact that the films were deposited under UHV conditions, the only possible source of such a high concentration of oxygen is the exposure to the ambient atmosphere during the transport and the storage of the films. Unlike bulk HfNbTaTiZr alloys prepared by conventional arc melting, which exhibit typical dendritic structure, EDS mapping of HEA films showed no segregation of Hf, Nb, Ta, Ti, Zr elements. Figure 5 shows EDS maps of the HEAM2 film, each point corresponds to an area with 60 nm diameter. Therefore, we can say the films are homogeneous on the scale larger than 100 nm, which is comparable with the size of the aggregate structure observed by AFM.

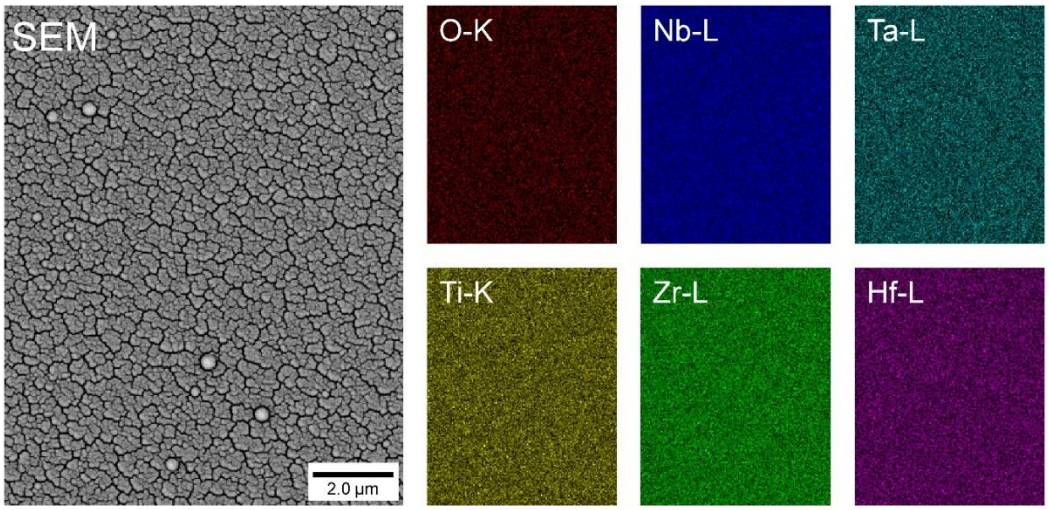

Figure 5: SEM picture (back-scattered electrons) and corresponding EDS maps of the O, Nb, Ta, Ti, Zr, and Hf elements for the HEAM2 film surface. K-lines were analyzed for O and Ti, L-lines were analyzed for Nb, Zr, Ta, and Hf.

The composition of HEA films was characterized by the XRF method. Note that XRF can be used for reliable determination of the concentration of chemical elements with Z > 10, i.e. it is not sensitive to oxygen content. The results of the XRF chemical analysis of HEAM1 and HEAM2 films are listed in Table 1. The results of the XRF chemical analysis of the HfNbTaTiZr target before and after sputtering are included in the table as well. The XRF spectra were treated within a model without calibrated standards, i.e. phenomena like X-ray absorption, self-excitation, and finite film thickness, were approximated by empirical formulas. Variation of atomic concentrations obtained by such a model is typically 2 – 5 at. %, depending on the parameters of the XRF model. Note that using a calibrated samples as standards can improve the precision of the XRF analysis 10 – 100 times and will be necessary for the authors' following studies concerning the composition of HEA films.

One can see in Table 1 that the composition of HEAM1 and HEAM2 films is, within the precision of the XRF analysis, close to the equimolar composition of the HfNbTaTiZr alloy. However, the HEAM1 film is enriched with Ti, while the HEAM2 film is depleted with Ti. The reason for this discrepancy is as follows. The first HEAM1 film was deposited from the original equimolar HfNbTaTiZr target. Ti enrichment of the film is caused by preferential sputtering of the Ti as the element with the lowest atomic mass. Simultaneously the target was depleted in Ti, as confirmed by the XRF analysis of the sputtered target. Therefore, the sputtering of the Ti depleted target leads to the lack of Ti in the following samples, particularly the HEAM2 film.

Element	**Ti**	**Zr**	**Nb**	**Hf**	**Ta**
XRF analysis					

K-line energy (keV)		4.510	15.776	16.617	55.801	57.450
L-line energy (keV)		0.452	2.042	2.166	7.898	8.145
composition* (at. %)						
HEAM1	as-deposited	23	19	19	18	21
HEAM2	as-deposited	18	21	21	19	21
HfNbTaTiZr	target before dep.	20	20	20	20	20
HfNbTaTiZr	target after dep.	12	22	23	20	23
sputtering						
atomic number		22	40	41	72	73
atomic mass		47.880	91.220	92.906	178.49	180.948
sputtering yield (at. per ion)**		0.577	0.632	0.634	0.748	0.664

* Only Ti, Zr, Nb, Hf, Ta elements were taken into account.

** Sputtering yields for normal incidence of Ar^+ ions with 500 eV energy [37-39].

Table 1: Chemical composition in at. % as determined by XRF for amorphous HEAM1 and HEAM2 films and HfNbTaTiZr target before and after deposition. K-lines were analyzed for Ti, Zr, and Nb, L-lines were analyzed for Hf and Ta. Atomic numbers, atomic masses, and sputtering yields [37-39] in the number of atoms per Ar^+ ion are included.

Sputtering yields in Ar for the normal incidence for Ti, Zr, Nb, Hf, Ta are among the lowest across the periodic table [37-39]. Further, within these five elements, the actual values of the yield are very comparable, see Table 1, which favors the near-equimolar composition of the deposited film. Note that values in Table 1 correspond to the sputtering of pure materials and does not take into account mutual bonds in the HfNbTaTiZr alloy. The preferential sputtering of Ti, therefore, seemingly contradicts its lowest sputtering yield compared to the other elements and is presumably the result of the lowest atomic mass of Ti.

XPS spectra for the HEAM2 film, which are shown in Figure 6, were fitted in the KolXPD software using Shirley background and Voigt peaks for O 1s or Voigt doublets with appropriate spin-orbit splitting for metal oxides. Metallic states of the same core levels with highly asymmetric profiles were fitted with Doniach-Šunjić doublets convoluted with Gaussian function instead. Metal oxide signal contributions are identified as peaks shifted to higher binding energies in comparison with the metallic peaks; the larger is the chemical shift, the higher is the oxidation number. Peak parameters and their chemical shifts are consistent with the literature [30, 40-46].

core level	Ti $2p_{3/2}$	Nb $3d_{5/2}$	Zr $3d_{5/2}$	Ta $4f_{7/2}$	Hf $4f_{7/2}$	O 1s
reference values – binding energy (eV)						

metal	453.94	202.31	178.75	21.80	14.28	--
metal – LW	0.25	0.07	0.09	0.03	0.04	--
highest oxide	TiO_2 458.5 - 459.3	Nb_2O_5 207.3 - 208.2	ZrO_2 182.0 - 183.4	Ta_2O_5 26.3 - 27.2	HfO_2 16.6 – 17.9	--
HEAM2 as deposited – binding energy (eV)						
metal		202.9	179.2	22.5	14.5	***531.4***
metal oxide	458.5	**208.4**	**183.4**	**27.1**	**18.0**	*532.4*
	459.8	207.0				
HEAM2 after 7h depth profiling – binding energy (eV)						
metal	**454.1**	**202.6**	**178.9**	**22.1**	**14.2**	***531.4***
metal oxide	454.9	203.1	**179.7**	22.7	14.8	*533.1*
		203.4	183.7	27.4	18.0	*535.1*

Table 2: Binding energies in eV of metals' [40, 41] and metal oxides' [43, 44] major core levels frequently used for XPS analysis. The standard deviation of values in [40] is 0.06 eV, LW is the Lorentz natural line width [41]. Bold values correspond to the position of the dominant peak in the measured XPS spectrum.

As revealed by XPS, the surface region of the HEAM2 film is oxidized. All deposited elements are present in a form of oxides, the oxygen content was determined to 66 at. %. No oxide particles were observed by SEM, TEM nor XRD though. Thus, we assume the present oxides are ordered on a short-range scale of few nm only. The real surface of the metallic film typically contains adsorbents from the ambient atmosphere and an oxide-based passivation layer [47, 48]. The presence of ambient adsorbates is reflected in the carbon content of 12 at. % in the as-deposited film, while a high oxygen content corresponds also to the passivation layer.

To investigate the oxidation with a depth resolution, a standard depth profiling using Ar^+ sputtering in the XPS apparatus was performed. After 1 h of depth profiling, a 30 – 50 nm thick layer was removed from a region probed by XPS and the oxygen concentration slightly decreased to 48 at. %. The oxide states of elements diminished in favor of metallic states. Virtually all Nb and Ta atoms were already in the metallic state. On the contrary, Ti and particularly Zr and Hf atoms remained both in the oxide and the metallic states. This is due to the high affinity of these elements to oxygen given by their electronegativity, bond energy, crystal cohesive energy, etc., as described in [49-51].

After 7 h of depth profiling, a 200 – 350 nm thick layer was removed and oxygen content dropped to 18 at. %. Ti, Zr, and Hf atoms were present predominantly in metallic states. Nevertheless, the oxide and sub-oxide states of these elements were still present. Hf and Zr exhibit a high amount of sub-oxide states attributed to the first stage of Zr and Hf oxidation

into ZrO_x- and HfO_x-like states due to the high affinity of these elements to dissolved oxygen [43-46].

Therefore with increasing depth oxygen content is gradually decreasing. Absorbed oxygen atoms are preferentially bonded to Ti, Zr, and Hf more likely than to Nb and Ta. However, in higher depths, the film has a metallic character. The relatively high oxygen content in higher depths shows oxygen was able to diffuse through the passivation layer. This was enabled by an open structure of the amorphous film acting as a getter. Oxygen diffusion into polycrystalline HEA films studied by XPS depth profiling was reported in [26].

Atomic concentrations of the deposited elements as determined by XPS fall into the range of (20 ± 10) at. %. The more precise composition is provided by the XRF analysis as a method less sensitive to the surface, which may, in general, exhibit deviations from the bulk composition. Moreover, depth profiling by Ar^+ sputtering is accompanied by many effects, which alter the composition of the studied material as well. Consequently, uncertainties in the obtained compositions must be taken into consideration [52].

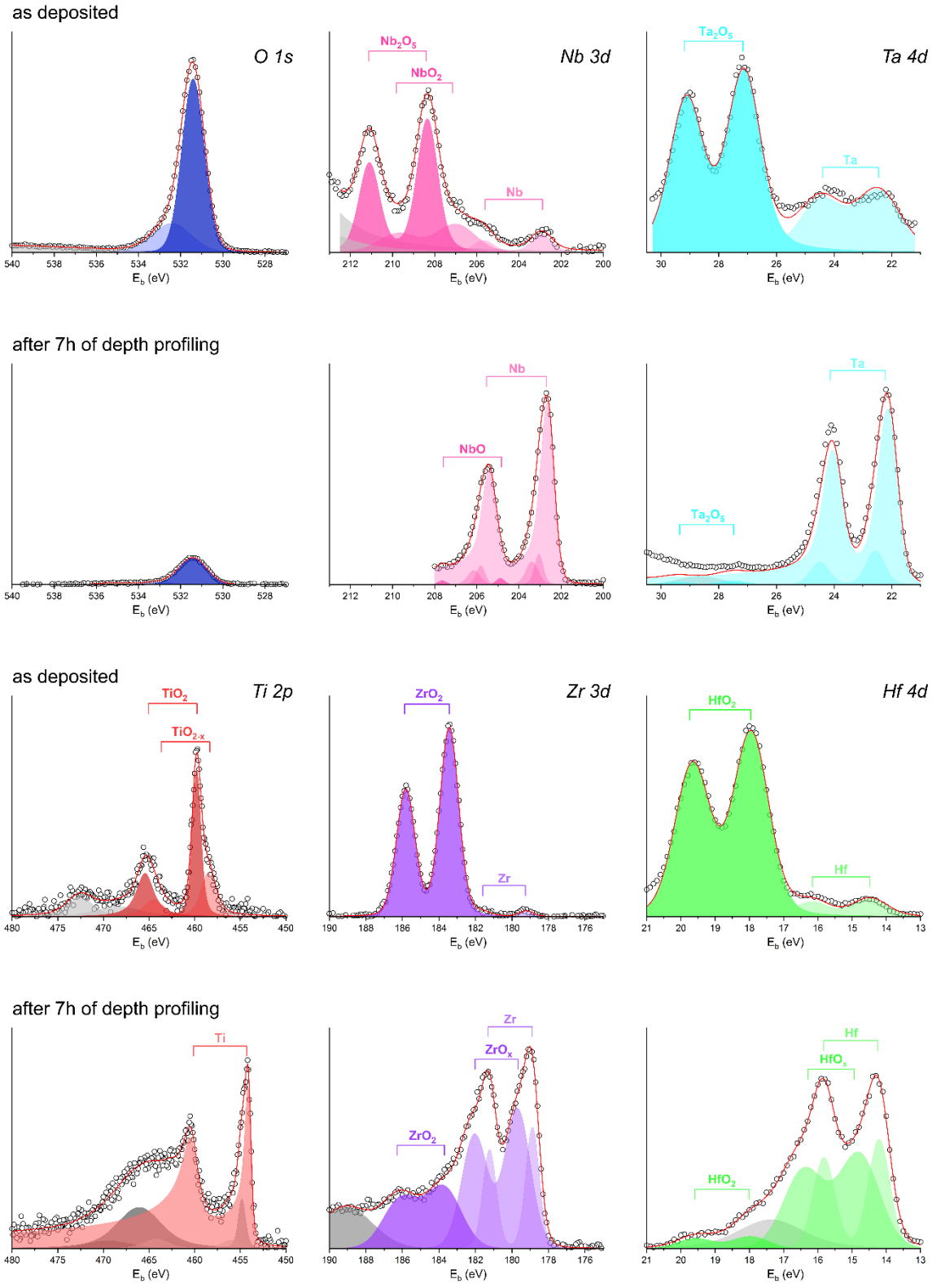

Figure 6: High-resolution XPS spectra of elements present in HEAM2 film measured in the as-deposited state and after 7 h of depth profiling. Measured data (open points) correspond well to the fit (red line). Positions of doublets for metal and oxide states are marked with horizontal lines.

The defect structure of a 1650 nm thick HEAM2 film was investigated by PALS. The positron implantation profile is described by the asymmetric Makhovian distribution. Both mean implantation depth $\bar{z}$ and FWHM w increase with positron energy with a power factor of 5/8. For simplicity, we propose using the interval $(1/2\,\bar{z}, 3/2\,\bar{z})$ to characterize the region, which contains 65 % of all implanted positrons. For the maximal positron energy of 16 keV, less than 10^{-7} % of all positrons penetrated the FS substrate. Therefore, all positrons annihilated in the volume of the film. Moreover, comparable depths of the HEAM2 sample were probed by the PALS and the XPS methods.

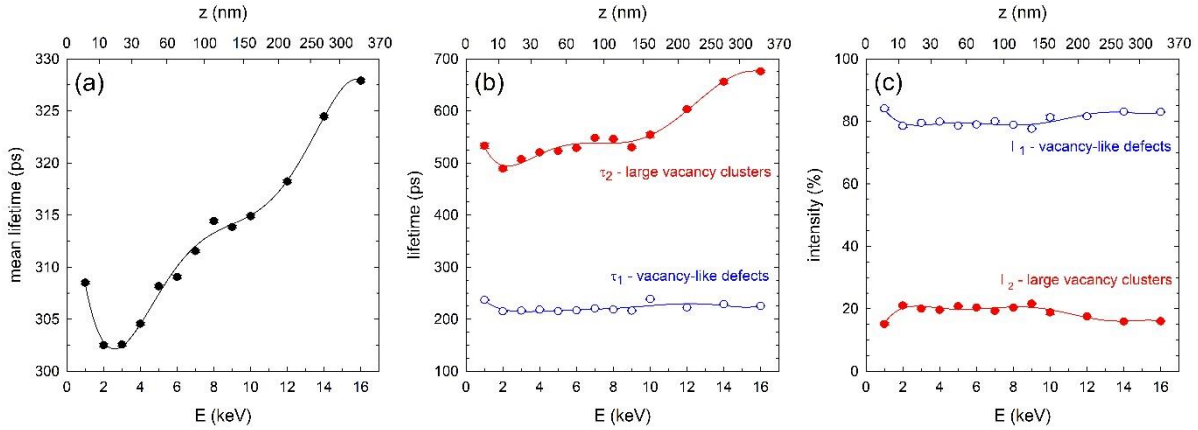

Figure 7: Positron lifetime measurements for the 1650 nm thick HEAM2 film plotted as a function of the energy of incident positrons, the mean positron penetration depth is depicted at the top axis. (a) Development of the mean positron lifetime, (b) positron lifetime components, and (c) their corresponding intensities.

In general, the mean positron lifetime $\bar{\tau}$ is a robust parameter, which is not influenced by mutual correlation among fitting parameters. Hence, the development of $\bar{\tau}$ provides an insight into the defect depth profile in the sample. Figure 7a shows $\bar{\tau}$ plotted as a function of the energy of incident positrons E, previously published in the authors' work [53]. For all energies the values of $\bar{\tau}$ exceed 300 ps, which is a much higher value than the bulk lifetime of 146 ps for HfNbTaTiZr alloy [54-56]. This is caused by vacancy-like open-volume defects, which are present in large concentrations and are able to trap thermalized positrons.

At very low energies (up to 1 keV) almost all positrons annihilated in the surface state. With increasing energy, positrons penetrate deeper into the HfNbTaTiZr layer, and a fraction of positrons diffusing back to the surface gradually decrease, which results in a decrease of $\bar{\tau}$. At higher energies (above 3 keV) $\bar{\tau}$ monotonically increase with energy. In general, the increase of the mean positron lifetime can be caused either by increasing concentration of vacancy-like defects or by an increase of their mean size.

To obtain a better insight into PALS data, for each positron energy the positron lifetime spectrum was decomposed into two exponential components: (i) short-lifetime component $\tau_1 \approx 220$ ps with intensity $I_1 \approx 80$ %; (ii) long-lifetime component $\tau_2 \gtrsim 500$ ps with intensity $I_2 \approx 20$ %. The development of lifetimes and intensities of both components with energy E is shown in Figures 7b and 7c. Since lifetimes of both components are substantially higher than the bulk lifetime for the HfNbTaTiZr alloy, the concentration of defects in the HEAM2 film is so high that all positrons are annihilated in the trapped state, so-called saturated positron trapping.

According to *ab-initio* calculations, the lifetime of a positron trapped in a monovacancy in the bcc-HfNbTaTiZr lattice is 212 ps. Therefore, the shorter component τ_1 corresponds to positrons trapped in small open-volume defects with a size comparable with a monovacancy. The values of lifetime τ_1 and intensity I_1 virtually does not change with depth. In context with the AFM observations, we assume positrons are predominantly trapped in open spaces between amorphous clusters with a mean size of ~10 nm.

The longer component τ_2 comes from positrons trapped in large vacancy clusters and voids between the ~100 nm large aggregates, which were observed by AFM. Note that the maximum theoretical lifetime of positrons annihilating in large vacancy clusters is 500 ps. Thus, the long-lifetime component τ_2 includes also pick-off annihilations of ortho-positronium (o-Ps) with a typical lifetime of ~1 ns, in particular for the energies of 12 keV and higher.

The constant intensity of the long-lifetime component means the concentration of inter-aggregate voids is approximately constant with depth, which is in good agreement with AFM observations. However, increasing lifetime τ_2 implies an increasing volume of inter-aggregate voids. This effect is likely connected with oxygen absorption in these voids. The XPS analysis revealed there is a high concentration of oxygen in the HEA films which strongly decreases with the depth. Hence, it is likely that voids in the sub-surface region are filled by oxygen atoms which effectively reduce its free volume and, thereby, also the lifetime of positron trapped inside the void. Alternatively, the presence of oxygen and oxides in the voids' walls can effectively prevent the formation of the positronium leading to a shortening of the lifetime component τ_2.

One can see in Figure 7 the lifetime τ_2 is virtually constant up to the depth of 150 nm. It means in this sub-surface region the inter-aggregate voids are likely saturated with oxygen. With increasing depth, τ_2 begins to grow due to reduced oxygen concentration inside voids. This is in very good agreement with XPS observations. Note that constant lifetime τ_1 and intensity I_1 indicate no significant oxygen absorption inside the amorphous structure. Thus, oxygen contamination occurs on the interfaces among aggregates only.

4. Conclusions

Two HfNbTaTiZr films with thicknesses of 380 nm and 1650 nm were deposited at room temperature on fused silica substrates by DC magnetron sputtering. A single bcc phase target, prepared by spark plasma sintering, was used. Both films exhibit an amorphous structure with no long-range ordering of atoms, as confirmed by TEM and XRD. A substructure of ~10 nm round clusters aggregating into ~100 nm formations was observed by AFM. The films' composition, according to XRF and EDS, is close to equimolar with slight Ti enrichment and no mutual segregation of elements.

Oxidation of the films was studied by XPS combined with depth profiling. Oxygen absorbed from the ambient atmosphere reacted with Ti, Zr, Nb, Hf, and Ta atoms and formed oxide and sub-oxide nanoclusters. The oxygen-contaminated layer with a thickness of approximately 200 – 350 nm, out of the total film thickness of 1650 nm, contains predominantly Ti, Zr, and Hf oxides. Two types of open volumes, uniformly distributed with depth, were observed by PALS. Larger open volumes, located in between the aggregates of amorphous round clusters, are a dominant region, where oxidation takes place. Smaller defects with a size comparable with a monovacancy in bcc HfNbTaTiZr structure are the dominant type of defects and are not influenced by oxygen content in the film. The presence of a high concentration of vacancy-like defects in the films may be feasible for hydrogen absorption.

The present study brings a new light on defects present in thin films of amorphous HfNbTaTiZr high entropy alloys. The element selective oxidation of topmost surface layers at room temperature was investigated by a combination of XPS (chemistry), PALS (defects), and AFM (topology). Obtained results showed that oxidation is an important issue in HfNbTaTiZr thin films and it is difficult to avoid penetration of oxygen into the film. In addition, it has been demonstrated that amorphous HfNbTaTiZr films contain nanoscopic open volumes. Such microstructure is favorable for hydrogen absorption. The potential of amorphous multicomponent concentrated alloys for hydrogen storage applications needs to be investigated in the future.

5. Acknowledgments

This work was supported by the Czech Science Foundation (project 17-17016S). P. Hruška acknowledges the support of the PPLZ project of the Czech Academy of Sciences. We acknowledge the Operational Program Research, Development and Education financed by European Structural and Investment Funds and the Czech Ministry of Education, Youth and Sports (Project SOLID21 CZ.02.1.01/0.0/0.0/16_019/0000760). Author P. Minárik acknowledges partial financial support by ERDF under project No. CZ.02.1.01/0.0/0.0/15 003/0000485. The MePS facility has partly been funded by the Federal Ministry of Education and Research (BMBF) with the grant PosiAnalyse (05K2013).

References

1. Miracle, D.B. and O.N. Senkov, *A critical review of high entropy alloys and related concepts.* Acta Materialia, 2017. **122**: p. 448-511.
2. Shi, P., et al., *Enhanced strength-ductility synergy in ultrafine-grained eutectic high-entropy alloys by inheriting microstructural lamellae.* Nat Commun, 2019. **10**(1): p. 489.
3. Lee, C., et al., *Lattice distortion in a strong and ductile refractory high-entropy alloy.* Acta Materialia, 2018. **160**: p. 158-172.
4. Zhang, Y., et al., *Microstructures and properties of high-entropy alloys.* Progress in Materials Science, 2014. **61**: p. 1-93.
5. Senkov, O.N., et al., *Microstructure and room temperature properties of a high-entropy TaNbHfZrTi alloy.* Journal of Alloys and Compounds, 2011. **509**(20): p. 6043-6048.
6. Cantor, B., *Multicomponent and High Entropy Alloys.* Entropy, 2014. **16**(9): p. 4749-4768.
7. Schuh, B., et al., *Thermodynamic instability of a nanocrystalline, single-phase TiZrNbHfTa alloy and its impact on the mechanical properties.* Acta Materialia, 2018. **142**: p. 201-212.
8. Brechtl, J., et al., *A Review of the Serrated-Flow Phenomenon and Its Role in the Deformation Behavior of High-Entropy Alloys.* Metals, 2020. **10**(8).
9. Senkov, O.N., et al., *Microstructure and elevated temperature properties of a refractory TaNbHfZrTi alloy.* Journal of Materials Science, 2012. **47**(9): p. 4062-4074.
10. El-Atwani, O., et al., *Outstanding radiation resistance of tungsten-based high-entropy alloys.* Sci Adv, 2019. **5**(3): p. eaav2002.
11. Islak, S., et al., *Wear properties and synthesis of CrFeNiMoTi high entropy alloy coatings produced by TIG process.* Indian Journal of Engineering & Materials Sciences, 2020. **27**: p. 659-664.
12. Zýka, J., et al., *Microstructure and Room Temperature Mechanical Properties of Different 3 and 4 Element Medium Entropy Alloys from HfNbTaTiZr System.* Entropy, 2019. **21**(2).
13. Dirras, G., et al., *Elastic and plastic properties of as-cast equimolar TiHfZrTaNb high-entropy alloy.* Materials Science and Engineering: A, 2016. **654**: p. 30-38.
14. Sahlberg, M., et al., *Superior hydrogen storage in high entropy alloys.* Sci Rep, 2016. **6**: p. 36770.
15. Zlotea, C., et al., *Hydrogen sorption in TiZrNbHfTa high entropy alloy.* Journal of Alloys and Compounds, 2019. **775**: p. 667-674.
16. Kirchheim, R., *Hydrogen solubility and diffusivity in defective and amorphous metals.* Progress in Materials Science, 1988. **32**(4): p. 261-325.
17. Pundt, A. and R. Kirchheim, *HYDROGEN IN METALS: Microstructural Aspects.* Annual Review of Materials Research, 2006. **36**(1): p. 555-608.
18. Hruška, P., et al., *Characterization of defects in titanium created by hydrogen charging.* International Journal of Hydrogen Energy, 2017. **42**(35): p. 22557-22563.
19. Guo, S., et al., *More than entropy in high-entropy alloys: Forming solid solutions or amorphous phase.* Intermetallics, 2013. **41**: p. 96-103.
20. Braeckman, B.R. and D. Depla, *On the amorphous nature of sputtered thin film alloys.* Acta Materialia, 2016. **109**: p. 323-329.
21. Braeckman, B.R., et al., *High entropy alloy thin films deposited by magnetron sputtering of powder targets.* Thin Solid Films, 2015. **580**: p. 71-76.

22. Braeckman, B.R. and D. Depla, *Structure formation and properties of sputter deposited Nbx-CoCrCuFeNi high entropy alloy thin films.* Journal of Alloys and Compounds, 2015. **646**: p. 810-815.
23. Tüten, N., et al., *Microstructure and tribological properties of TiTaHfNbZr high entropy alloy coatings deposited on Ti 6Al 4V substrates.* Intermetallics, 2019. **105**: p. 99-106.
24. Motallebzadeh, A., et al., *Mechanical Properties of TiTaHfNbZr High-Entropy Alloy Coatings Deposited on NiTi Shape Memory Alloy Substrates.* Metallurgical and Materials Transactions A, 2018. **49**(6): p. 1992-1997.
25. Kim, Y.S., et al., *Investigation of structure and mechanical properties of TiZrHfNiCuCo high entropy alloy thin films synthesized by magnetron sputtering.* Journal of Alloys and Compounds, 2019. **797**: p. 834-841.
26. Cropper, M.D., *Thin films of AlCrFeCoNiCu high-entropy alloy by pulsed laser deposition.* Applied Surface Science, 2018. **455**: p. 153-159.
27. Lukac, F., et al., *Spark plasma sintering of gas atomized high-entropy alloy HfNbTaTiZr.* Journal of Materials Research, 2018. **33**(19): p. 3247-3257.
28. Coelho, A.A., *TOPASandTOPAS-Academic: an optimization program integrating computer algebra and crystallographic objects written in C++.* Journal of Applied Crystallography, 2018. **51**(1): p. 210-218.
29. Yeh, J.J. and I. Lindau, *Atomic subshell photoionization cross sections and asymmetry parameters: 1 ⩽ Z ⩽ 103.* Atomic Data and Nuclear Data Tables, 1985. **32**(1): p. 1-155.
30. Moulder, J.F., J. Chastain, and R.C. King, *Handbook of x-ray photoelectron spectroscopy: a reference book of standard spectra for identification and interpretation of XPS data*. 1995: Eden Prairie Minnesota: Physical Electronics.
31. Wagner, A., et al., *Positron annihilation lifetime and Doppler broadening spectroscopy at the ELBE facility* AIP Conference Proceedings, 2018. **1970**: p. 040003
32. Gabriel, F., et al., *The Rossendorf radiation source ELBE and its FEL projects.* Nuclear Instruments and Methods in Physics Research Section B: Beam Interactions with Materials and Atoms, 2000. **161-163**: p. 1143-1147.
33. Schultz, P.J. and K.G. Lynn, *Interaction of positron beams with surfaces, thin films, and interfaces.* Reviews of Modern Physics, 1988. **60**(3): p. 701-779.
34. Čížek, J., *PLRF Code for Decomposition of Positron Lifetime Spectra.* Acta Physica Polonica A, 2020. **137**(2): p. 177-187.
35. Lan, S., et al., *Structure origin of a transition of classic-to-avalanche nucleation in Zr-Cu-Al bulk metallic glasses.* Acta Materialia, 2018. **149**: p. 108-118.
36. Ma, D., A.D. Stoica, and X.L. Wang, *Power-law scaling and fractal nature of medium-range order in metallic glasses.* Nat Mater, 2009. **8**(1): p. 30-4.
37. Matsunami, N., et al., *Energy dependence of the ion-induced sputtering yields of monatomic solids.* Atomic Data and Nuclear Data Tables, 1984. **31**(1): p. 1-80.
38. Seah, M.P., et al., *An accurate semi-empirical equation for sputtering yields I: for argon ions.* Surface and Interface Analysis, 2005. **37**(5): p. 444-458.
39. NPL. *Sputter yield values*. 2020; Available from: https://www.npl.co.uk/research/mass-spectrometry/secondary-ion/sputter-yield-values.
40. Powell, C.J., *Recommended Auger parameters for 42 elemental solids.* Journal of Electron Spectroscopy and Related Phenomena, 2012. **185**(1-2): p. 1-3.
41. Campbell, J.L. and T. Papp, *Widths of the Atomic K–N7 Levels.* Atomic Data and Nuclear Data Tables, 2001. **77**(1): p. 1-56.

42. Biesinger, M.C. *X-ray Photoelectron Spectroscopy (XPS) Reference Pages*. 2020; Available from: http://www.xpsfitting.com.
43. Jayaraj, J., et al., *Corrosion behavior and surface film characterization of TaNbHfZrTi high entropy alloy in aggressive nitric acid medium.* Intermetallics, 2017. **89**: p. 123-132.
44. Morant, C., L. Galán, and J.M. Sanz, *An XPS study of the initial stages of oxidation of hafnium.* Surface and Interface Analysis, 1990. **16**(1-12): p. 304-308.
45. Bespalov, I., et al., *Initial stages of oxide formation on the Zr surface at low oxygen pressure: An in situ FIM and XPS study.* Ultramicroscopy, 2015. **159 Pt 2**: p. 147-51.
46. Ma, W., et al., *Non-equilibrium oxidation states of zirconium during early stages of metal oxidation.* Applied Physics Letters, 2015. **106**(10).
47. Greenwood, N.N. and A. Earnshaw, *Chemistry of the Elements*. 2nd ed. 1997: Elsevier. 1600.
48. Schweitzer, P.A., *Metallic materials: Physical, Mechanical, and Corrosion Properties*. 2003, New York: Marcel Dekker, Inc.
49. Backman, L. and E.J. Opila, *Thermodynamic assessment of the group IV, V and VI oxides for the design of oxidation resistant multi-principal component materials.* Journal of the European Ceramic Society, 2019. **39**(5): p. 1796-1802.
50. Backman, L., et al., *Part I: Theoretical predictions of preferential oxidation in refractory high entropy materials.* Acta Materialia, 2020. **197**: p. 20-27.
51. Backman, L., et al., *Part II: Experimental verification of computationally predicted preferential oxidation of refractory high entropy ultra-high temperature ceramics.* Acta Materialia, 2020. **197**: p. 81-90.
52. Watts, J.F. and J. Wolstenholme, *An Introduction to Surface Analysis by XPS and AES*. 2019: Wiley.
53. Lukáč, F., et al., *Defects in Thin Layers of High Entropy Alloy HfNbTaTiZr.* Acta Physica Polonica A, 2020. **137**(2): p. 219-221.
54. Lukáč, F., et al., *Defects in High Entropy Alloy HfNbTaTiZr Prepared by High Pressure Torsion.* Acta Physica Polonica A, 2018. **134**(3): p. 891-894.
55. Čížek, J., et al., *Strength enhancement of high entropy alloy HfNbTaTiZr by severe plastic deformation.* Journal of Alloys and Compounds, 2018. **768**: p. 924-937.
56. Kuriplach, J., et al., *Behavior of Positrons in the HfNbTaTiZr Complex Concentrated Alloy.* Acta Physica Polonica A, 2020. **137**(2): p. 260-265.